DOCTORAL THESIS

Investigating the electro-optical properties of 3D superlattices and 2D materials: A DFT study

A thesis submitted to the Institute of Physics, Polish Academy of Sciences in partial fulfillment of the requirements for the degree Doctor of Philosophy supervised by Dr. hab. Carmine Autieri, prof. IFPAN and auxiliary supervisor Dr. Giuseppe Cuono.

By

Ghulam Hussain

Institute of Physics, Polish Academy of Sciences
Warsaw Poland

January 2023

Dedication and acknowledgements

I would like to say special thanks to my supervisor Dr. Carmine Autieri for his continuous support and guidance throughout my PhD. In addition, I am very thankful to Prof. Tomasz Dietl and my co-guide Dr. Giuseppe Cuono for their assistance and constructive suggestions. Last but not the least, I pay gratitude to my friends and my beloved family, without whose endless love, encouragement and support, I could not achieve this.

Moreover, we appreciate the support of the Foundation for Polish Science through the international research agendas program co-financed by the European Union within the smart growth operational program.

Author's declaration

I hereby certify that the work contained in this dissertation has not been submitted for consideration in any other academic awards and has been completed in accordance with the rules and guidelines of the Institute of Physics, Polish Academy of Science (IFPAN) and the Code of Practice for Research Degree Programs. Unless otherwise specified by a specific reference in the text, the work is the candidate's own contribution. Work accomplished with the assistance of or in collaboration with others is acknowledged as such. In the dissertation, only the author's viewpoints are given.

SIGNED: ..... DATE: .....

List of publications

This thesis includes the following papers, where I contributed as the 1st author highlighted by bold text.

Ghulam Hussain, Giuseppe Cuono, Rajibul Islam, Artur Trajnerowicz, Jarosław Jureńczyk, Carmine Autieri, Tomasz Dietl. *Electronic and optical properties of InAs/$InAs_{0.625}Sb_{0.375}$ superlattices and their application to far-infrared detectors,* Journal of Physics D: Applied physics **55**, 495301 (2022)

Ghulam Hussain, Mazia Asghar, Muhammad Waqas Iqbal, Hamid Ullah, Carmine Autieri. *Exploring the structural stability, electronic and thermal attributes of synthetic 2D materials and their heterostructures*, Applied Surface Science **590**, 153131 (2022)

Ghulam Hussain, Mumtaz Manzoor, Muhammad Waqas Iqbal, Imran Muhammad, Asadollah Bafekry, Hamid Ullah, Carmine Autieri. *Strain modulated electronic and optical properties of laterally stitched $MoSi_2N_4/XSi_2N_4$ (X=W, Ti) 2D heterostructures,* Physica E **144**, 115471 (2022)

Ghulam Hussain, Abdus Samad, Majeed Ur Rehman, Giuseppe Cuono, Carmine Autieri. *Emergence of Rashba splitting and spin-valley properties in Janus $MoGeSiP_2As_2$ and $WGeSiP_2As_2$ monolayers,* Journal of Magnetism and Magnetic Materials **563**, 169897 (2022)

Publications other than thesis

I also contributed in the following papers.

Giuseppe Cuono, **Ghulam Hussain**, Amar Fakhredine, and Carmine Autieri. *Topological phase diagram of $Pb_{1-x}Sn_xSe_{1-y}Te_y$ quaternary compound* (Accepted in Acta Physics Polonica A)

Rajibul Islam, **Ghulam Hussain**, Rahul Verma, Mohammad Sadegh Talezadehlari, Zahir Muhammad, Bahadur Singh and Carmine Autieri. *Electrically-controllable large gap quantum spin Hall phase in MGe_2Z_4* (Submitted)

Mian Muhammad Faisal, Syeda Ramsha Ali, **Ghulam Hussain**, Carmine Autieri, Sanal Kozhiparambil Chandran. *Development of 2D W_2CT_x MXene from non-MAX Phase W-Sn-C for Electrochemical Energy Storage Devices: Experiment and theory* (Submitted)

Zahir Muhammad, Faiz Wali, **Ghulam Hussain**, Rajibul Islam, Sami Ullah, Carmine Autieri, Peng Wu, Firoz Khan, Yue Zhang, Thamraa Alshahrani, and Weisheng Zhao. *Anisotropic phonon dispersion and optoelectronic properties of a few layers HfS_2*, J. Mater. Chem. C, (2023)

CERTIFICATE

This is to certify that the thesis entitled “Investigating the electro-optical properties of 3D superlattices and 2D materials: A DFT study”, submitted by Ghulam Hussain to Institute of Physics, Polish academy of sciences, is a record of bona fide research work under our supervision and guidance, and we consider it worthy of consideration for the award of the degree of Doctor of Philosophy of the Institute.

Supervisor

Dr. hab. Carmine Autieri, prof. IFPAN
MagTop, Institute of Physics, Polish academy of sciences
Warsaw, Poland

Auxiliary supervisor

Dr. Giuseppe Cuono
MagTop, Institute of Physics, Polish academy of sciences
Warsaw, Poland

ABSTRACT

The electromagnetic radiations can propagate in space, which could interact with the matter in various ways. Advancement in the electronic industry demands to explore new materials with pronounce electronic and optical features. Due to the boosted semiconductor industry, the optoelectronic devices are extensively employed in manufacture, medicine, astronomy, automobile, communications, military, and so on, reshaping our lives. These include light emitting diodes, semiconducting lasers, photovoltaic devices, photodiodes and photodetectors. Previous studies incorporate the investigation of optoelectronic properties for different materials such bulk systems, alloys, thin films and 2D layered structures. Currently, the Ga- and Hg-free type-II superlattices of InAs/(InAsSb) are highly demanding in the infrared industry due to their unique optoelectronic properties. Moreover, the distinct mechanical and electro-optical features of the newly discovered 2D materials family MA_2Z_4 as compared to other 2D materials necessitates further studies to explore this 2D material class.

Motivated from the outstanding characteristics of Ga- and Hg-free type-II superlattices of InAs/(InAsSb), and the extraordinary mechanical and electro-optical features of MA_2Z_4 family, we explore here the electronic and optical properties of InAs/$InAs_{0.625}Sb_{0.375}$ 3D superlattice (SL), 2D materials XSi_2N_4 (X = Mo, W, and Ti) and their vertical/lateral heterostructures $MoSi_2N_4$/XSi_2N_4 (W, Ti), and Janus structures.

In the study of InAs/$InAs_{0.625}Sb_{0.375}$ 3D superlattice, the modified Becke-Johnson exchange-correlation functional is employed to have a good description of the electronic and optical properties. The bulk InAs and InSb are analyzed first and then the InAs/$InAs_{0.625}Sb_{0.375}$ superlattice for the three lattice constants of the bulk InAs, GaSb and AlSb is investigated, respectively. A strong dependence of electronic and optical properties on the variation of lattice constant is observed. There exists two heavy-hole bands with increasing in-plane effective mass as one goes far from the Fermi level. In addition, a considerable decrease in the effective masses for heavy-holes and energy gaps in the k_x-k_y plane is noticed as compared to their bulk phases of the parent compounds. We noticed that the electrons are delocalized in the InAs part of SL, while the holes mainly are localized in the $InAs_{0.625}Sb_{0.375}$ part. The absorption spectra in the far-infrared regime are strongly increased in the case of the aforementioned superlattice with respect to bulk InAs and InSb suggesting their applications in long-wavelength IR detectors.

In the second project, we discuss newly discovered 2D layered materials such as XSi_2N_4 (X = Mo, W, and Ti), and their vertical and laterally stitched 2D heterostructures $MoSi_2N_4$/XSi_2N_4 (X=W, Ti). We report that all the systems are structurally stable as confirmed by the total energy ground state calculations and the phonon spectra. After establishing their thermodynamical stability, we study the electronic band structures and the density of states of the monolayers XSi_2N_4 (X = Mo, W, and Ti) and 2D heterostructures, respectively. Both the monolayers and the heterostructures demonstrate a semiconducting behavior with band gaps ranging from the infrared to the visible

region. From the electronic band structures, we noticed that the band gap of $MoSi_2N_4/WSi_2N_4$ lies in the visible region employing their applications for photovoltaics and other optoelectronic devices. Instead, in the $MoSi_2N_4/TiSi_2N_4$ wherein the 'W' is replaced with 'Ti', the band gap drops to the IR range, thus providing the possibility to utilize these heterostructures as IR detector materials. In the third project, we extend the study of laterally stitched 2D heterostructures to investigate the effect of biaxial strain on the electronic and optical properties, which reveals significant modifications in the electronic band structures and optical spectra. We observed a transition from indirect to direct band gap semiconductor with the compressive strain in $MoSi_2N_4/WSi_2N_4$. Similarly, the biaxial strain causes a semiconducting to metallic transition in $MoSi_2N_4/TiSi_2N_4$. Besides, the optical spectra including absorbance, transmittance and reflectance can be tuned effectively using strain engineering. Our findings based on the electro-optical properties and their controlled modulation via biaxial strain suggest that these newly discovered 2D materials and heterostructures could be useful in nano- and optoelectronics.

Lastly, we study the pristine $MoSi_2P_4$ and Janus phase $XGeSiP_2As_2$ (Mo, W) in this new family of 2D materials. The appearance of high cohesive energies and the absence of imaginary phonon modes confirm their stability and possible experimental realization. The Janus structures indicate small direct band gaps and larger spin splittings at K/K’ in comparison to pristine $MoSi_2P_4$. The monolayered structure of Janus material possesses the broken mirror symmetry that gives rise to a potential gradient, which is normal to the plane of the material. This generates a difference in the work function of 2D material for the two surfaces. In addition, it is exposed from the spin textures that the broken mirror symmetry causes the Rashba spin-splitting in the Janus monolayers, which can be increased by using higher atomic spin-orbit coupling. In the supplementary material, we manifest and compare the optical spectra for pristine and Janus phases revealing characteristic absorption peaks in the infrared region. The large spin and Rashba-type splittings together with the exceptional optical spectra in the Janus structures can make an extraordinary contribution to the valleytronics, spintronics and IR applications.

ABSTRAKT

Promieniowanie elektromagnetyczne może rozchodzić się w przestrzeni oddziaływując z materią na wiele sposobów. Postęp w przemyśle elektronicznym wymaga poszukiwania nowych materiałów o specyficznych własnościach elektronowych i optycznych. Urządzenia optoelektroniczne, takie jak diody elektroluminescencyjne, lasery półprzewodnikowe, urządzenia fotowoltaiczne, fotodiody i fotodetektory, są szeroko stosowane w przemyśle, medycynie, astronomii, motoryzacji, komunikacji, wojsku itd., mając duży wpływ na nasze życie. Wcześniejsze prace badawcze dotyczyły właściwości optoelektronicznych różnego rodzaju materiałów, takich jak stopy, cienkie warstwy i inne struktury warstwowe 2D. Obecnie supersieci typu II InAs/(InAsSb) wolne od Ga i Hg są bardzo pożądane dla zastosowań w podczerwieni ze względu na ich unikalne właściwości optoelektroniczne. Z drugiej strony właściwości mechaniczne i elektrooptyczne nowo odkrytej rodziny materiałów 2D MA_2Z_4 predestynują je do zastosowań komercyjnych, ale konieczne są dalsze badania dla scharakteryzowania tej klasy materiałów 2D.

Motywowani nietypowymi właściwościami supersieci typu II bez Ga i Hg InAs / (InAsSb) oraz właściwościami mechanicznymi i elektrooptycznymi rodziny MA_2Z_4, badamy właściwości elektronowe i optyczne supersieci 3D InAs/$InAs_{0,625}Sb_{0,375}$ (SL), materiałów 2D XSi_2N_4 (X = Mo, W i Ti) oraz ich pionowe/boczne heterostruktury $MoSi_2N_4$/XSi_2N_4 (W, Ti) oraz struktury typu Janus.

W badaniu supersieci 3D InAs/$InAs_{0,625}Sb_{0,375}$ zastosowano zmodyfikowany funkcjonał korelacji wymiany Becke-Johnsona, aby uzyskać dobry opis właściwości elektronowych i optycznych. Najpierw analizujemy objętościowe układy InAs i InSb, a następnie badamy supersieci InAs/$InAs_{0,625}Sb_{0,375}$ dla trzech różnych stałych sieciowych: InAs, GaSb i AlSb. Obserwujemy silną zależność właściwości elektronowych i optycznych od wielkości stałej sieciowej. Otrzymujemy dwa pasma ciężkich dziur o rosnącej efektywnej masie w płaszczyźnie w miarę oddalania się od poziomu Fermiego. Ponadto zauważalny jest znaczny spadek mas efektywnych dla ciężkich dziur i przerw energetycznych w płaszczyźnie k_x-k_y w porównaniu z fazami objętościowymi związków macierzystych. Zauważyliśmy, że elektrony są zdelokalizowane w części InAs SL, podczas gdy dziury są zlokalizowane głównie w części $InAs_{0,625}Sb_{0,375}$. Widma absorpcyjne w dalekiej podczerwieni są silnie wzmocnione w porównaniu do objętościowych InAs i InSb, co sugeruje ich zastosowanie w długofalowych detektorach IR.

W drugim projekcie omawiamy nowo odkryte materiały warstwowe 2D, takie jak XSi_2N_4 (X = Mo, W i Ti) oraz ich pionowo i poprzecznie skonfigurowane heterostruktury 2D $MoSi_2N_4$/XSi_2N_4 (X=W, Ti). Okazuje się, że wszystkie systemy są strukturalnie stabilne, co potwierdzają obliczenia stanu podstawowego całkowitej energii i widma fononów. Po ustaleniu ich stabilności termodynamicznej badamy odpowiednio struktury pasm elektronowych i gęstość stanów monowarstw XSi_2N_4 (X = Mo, W i Ti) oraz heterostruktur 2D. Zarówno monowarstwy, jak i

heterostruktury wykazują właściwości półprzewodnikowe z pasmami wzbronionymi w zakresie od podczerwieni do obszaru widzialnego. Na podstawie struktur pasma elektronicznego zauważyliśmy, że pasmo wzbronione $MoSi_2N_4/WSi_2N_4$ leży w obszarze widzialnym, co pozwala na zastosowania w fotowoltaice i innych urządzeniach optoelektronicznych. Natomiast w $MoSi_2N_4/TiSi_2N_4$, gdzie wolfram zastąpiono tytanem, pasmo wzbronione przenosi się do zakresu IR, zapewniając w ten sposób możliwość wykorzystania tych heterostruktur jako detektorów IR. W trzecim projekcie rozszerzamy badanie heterostruktur 2D zszytych bocznie, aby zbadać wpływ odkształcenia dwuosiowego na właściwości elektroniczne i optyczne. Obserwujemy znaczące modyfikacje w strukturach pasm elektronowych i widmach optycznych, w tym przejście od pośredniego do bezpośredniego półprzewodnika z pasmem wzbronionym przy naprężeniu ściskającym w $MoSi_2N_4/WSi_2N_4$. Podobnie odkształcenie dwuosiowe powoduje przejście półprzewodnikowe do metalicznego w $MoSi_2N_4/TiSi_2N_4$. Poza tym widma optyczne, w tym absorbancję, transmitancję i współczynnik odbicia, można skutecznie dostroić za pomocą manipulacji odkształceniem. Nasze badania właściwościach elektrooptycznych i ich kontrolowanej modulacji przez odkształcenie dwuosiowe sugerują, że te nowo odkryte materiały i heterostruktury 2D mogą być przydatne w nano- i optoelektronice.

Badamy również czysty $MoSi_2P_4$ i oraz fazę typu Janus $XGeSiP_2As_2$ (Mo, W). Pojawienie się wysokich energii kohezji i brak urojonych modów fononów potwierdza ich stabilność i sugeruje możliwość przeprowadzenia badań doświadczalnych. Struktury typu Janus wykazują w porównaniu z czystym $MoSi_2P_4$ małe bezpośrednie przerwy wzbronione i większe rozszczepienie spinowe przy K/K'. Jednowarstwowa struktura materiału Janus posiada złamaną symetrię lustrzaną, co powoduje powstanie gradientu potencjału, który jest normalny do płaszczyzny materiału. Generuje to różnicę w funkcji pracy materiału 2D dla dwóch powierzchni. Ponadto z tekstur spinowych wynika, że złamana symetria lustrzana powoduje w monowarstwach typu Janus rozszczepienie spinowe Rashby, które można zwiększyć stosując wyższe atomowe sprzężenie spinowo-orbitalne. W dodatkowym materiale przedstawiamy i porównujemy widma optyczne dla faz czystej i typu Janus, ujawniając charakterystyczne piki absorpcji w obszarze podczerwieni. Duże rozszczepienia spinowe i typu Rashby w połączeniu z wyjątkowymi widmami optycznymi w strukturach Janus mogą być bardzo przydatne w Valleytronice, Spintronice i zastosowaniach w podczerwieni.

Table of Contents

List of Figures

Chapter 1

INTRODUCTION

The electronic and optical properties are of extreme importance while designing the electronic devices for optoelectronic applications. In optoelectronics, the investigation and utilization of materials is carried out that could 1) produce or become the source of light, 2) detect the light [1]. In the first instance, the electronic devices such as light emitting diodes (LEDs) and the semiconducting lasers are widely employed, which convert the electrical signals into light energy. On the other hand, for the detection purpose devices like photodiodes and photodetectors are commonly used, that convert the light energy into electrical signals. Besides, solar cells are commercially utilized in different parts of the world as a renewable source of energy that convert the sunlight into useful electrical energy through the photovoltaic effect. Owing to the importance of optoelectronics, the investigation of new materials for the electronic and optical features is quite demanding.

To this end, we first explore the $InAs/InAs_{0.625}Sb_{0.375}$ 3D superlattice (SL) and then 2D materials, which include XSi_2N_4 (X = Mo, W, and Ti) monolayers and their vertical/lateral heterostructures (such as $MoSi_2N_4/WSi_2N_4$, and $MoSi_2N_4/TiSi_2N_4$), and the Janus structures $XGeSiP_2As_2$ (X = Mo, W). The thesis comprises four chapters, **chapter 1** that is devoted to introduction, while the methodology is explained in **chapter 2**, **chapter 3** consists of results and discussion, where we include four published papers, and the last **chapter 4** covers conclusions.

In paper I, we investigate the electronic and optical properties of the bulk InAs, InSb and that of $InAs/InAs_{0.625}Sb_{0.375}$ SL and emphasizes why the $InAs/InAs_{0.625}Sb_{0.375}$ 3D superlattices are suitable for applications in far infrared detection. In paper II, we report the newly discovered 2D layered materials such as XSi_2N_4 (X = Mo, W, and Ti), and their vertical/lateral heterostructures like $MoSi_2N_4/WSi_2N_4$, and $MoSi_2N_4/TiSi_2N_4$. It is established that the monolayers as well as the heterostructures are structurally stable with unique electronic properties as confirmed from the density of states and electronic bandstructures. Both, the monolayers and the heterostructures demonstrate a semiconducting behavior with band gaps ranging from the infrared to the visible region. The paper III is the extension of paper II, where the effect of biaxial strain on the electro-optical properties of laterally stitched heterostructures is explored. The study revealed substantial modifications in the electronic and optical properties. In paper IV, the pristine $MoSi_2P_4$ and Janus $XGeSiP_2As_2$ (X = Mo, W) monolayers of new family of 2D materials are studied. The high

cohesive energies and the non-existence of imaginary phonon modes confirm their stabilities. The Janus structures $XGeSiP_2As_2$ (X = Mo, W) with broken mirror symmetry indicate small direct band gaps, larger spin splittings at K/K' and the Rashba spin-splitting in comparison to pristine $MoSi_2P_4$. From the electronic and optical band gaps, it is recognized that these materials can be used in near- and mid- infrared detection applications.

1.1 Motivation of $InAs/InAs_{0.625}Sb_{0.375}$ 3D SL

Infra-red are electromagnetic radiations lying just below the red color of the visible spectrum. An IR detector is a device, which in general images, detects, and/or measures the patterns of thermal radiations emitted by all objects. In the start, the development of IR sensors/detectors was linked with those of thermal detectors, for instance the bolometers and thermocouples. These detectors were operated at room temperature, which could sense almost the whole infrared spectrum of wavelengths, and are widely used even today. The second type is the photon detectors, which are more developed in terms of sensitivity and their response time. So far, several class of materials have been utilized in the IR technology, such as Pb salt, extrinsic Ge (doped with Cu, Zn, Au), InSb, InAs and their alloys, IV−VI alloy ($Pb_{1-x}Sn_xTe$), II−VI ($Hg_{1-x}Cd_xTe$), and GaAs/AlGaAs superlattices (SLs). However, there are always some drawbacks as will be discussed in the coming sections of this chapter. The experiments of Sir Frederick William Herschel in 1800, to measure the temperature of each color in the electromagnetic spectrum lead to the discovery of IR radiations. After measuring the temperature individually for colors such as red, orange, yellow, green, blue and violet, he noticed that the temperature in the visible range decreases from red to violet, and vice versa. After noticing such a trend of temperature, Herschel performed other experiments for measuring the temperature after red part of the visible spectrum; region of no sunlight. Surprisingly, he observed the highest temperature for this region. Further experiments revealed that these radiations can reflect, refract, transmit, and absorb just like visible light. This invisible light just beyond the red portion of the visible region is now termed as infrared radiation [2-4]. Figure 1.1 shows the schematic of electromagnetic spectrum, where the spectral window for infrared region is divided into three sub-spectral ranges i.e. from 0.7 to 3 μm that lies near IR (NIR), from 3 to 5 μm mid-wave IR (MWIR), and from 8 to 30 μm as long-wave IR (LWIR)/far IR (FIR). For example, the range of thermal radiations emitted by ordinary objects and human bodies lie in the FIR spectral window. Therefore, the tracking of thermal objects can be feasible with the design of LWIR cameras.

The first thermocouple and electrical thermometer were designed in 1829 by L. Nobili with the discovery of thermoelectric effect (Seebeck in 1826). After four years, M. Melloni connected in series many bismuth−copper based thermocouples, which generated measurable and higher output voltage. He found the device almost 40 times sensitive with respect to the available thermometers at that time, which can sense a person's heat who is at 30 ft distance from the detector [5]. In 1880, Samuel Pierpont Langley invented a bolometer that looked like a Wheatstone bridge [6, 7]. With this instrument, he was able to study the solar radiations at different wavelengths and the irradiance

in the IR range [8-10]. Langley continues efforts of developing and improving his bolometer yielding the detector to be 400 times more sensitive, which could even sense the thermal heat of a cow that is a quarter mile away from the bolometer [8]. The first observation of photoemission was revealed by Hertz in 1887, when he noticed the emission of negatively charged entities from a conductor by irradiating it with the UV light [11]. Further experiments indicated that the effect is also possible with the visible light by using alkali metal [12]. Between the WW I and WWII, the image converters and photon detectors were developed, together with the infrared spectroscopy, which was considered as important analytical tool for the chemists. The image converter (designed just before the WW II) was of immense importance to military, since this instrument enabled the night vision in the darkness. Theodore W. Case developed the first infrared photoconductor in 1917 [13], where the photoconductivity for Tl_2S was exhibited. The system was able to send messages to about 18 miles in the environment known as smoky atmosphere. During 1930's, in the United States perhaps the crucial development in the IR technology was the Radio Corporation of America (RCA) IR image tube. The NIR cathodes during WW II were connected with visible phosphors that provided the image converter in NIR. After setting up the National Defense Research Committee, the tube was produced in large productions as RCA 1P25 image converter in 1942. In the WW II, this tube connected to 'Sniperscope' and 'Snooperscope' were extensively benefited for night vision. At the University of Berlin, Edgar W. Kutzscher in 1933 observed that PbS is photoconductive, which can response to 3 μm. In 1943, the photoconductors based on PbS were brought into productions in Germany. This was the first ever practical IR detector (bearing excellent range) used during the WW II for various applications [14].

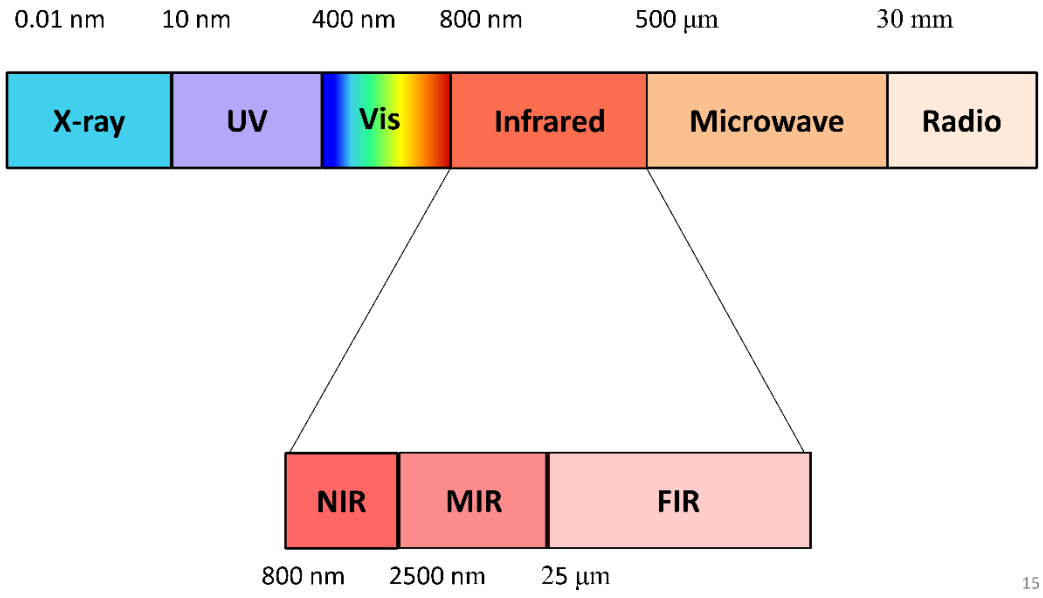

Figure 1.1 Electromagnetic spectrum increasing wavelength indicated from X-ray to radio, the infrared region is also zoomed with NIR, MWIR, and FIR shown.

In 1941, the thallous sulphide based detectors technology was improved by Robert J. Cashman leading to large production [15, 16]. After success, Cashman focused his studies on PbS based detectors. After WW II, he established that other semiconductors such as PbTe and PbSe can be used as infrared detectors [17]. It was only a matter of time before the military realized the benefits of night vision. At the end of World War II, IR technology for the military was still in its infancy. From the 1950s, passive night vision technology and the radiometric instruments were the key IR hardware developments, which enabled the vision in ambient starlight. After the war, the fire control, communications and the search systems strongly stimulated the lead salt detector technology development, which has continued even today. The IR systems, primarily for anti-air missile seekers, were constructed from cooled lead salt detectors [7]. For many applications in the spectral ranges 1-3 μm and 3-5 μm, the low-cost, adaptable PbS and PbSe polycrystalline thin films continue to be the preferred photoconductive detectors after 60 years. The focal plane arrays (FPAs) is the current lead salt development. Following the invention of the transistor, which greatly improved the growth and material purification procedures, extrinsic impurity based photoconductive detectors were reported in 1950s [18, 19]. These first extrinsic detectors were germanium based, since the methods for impurity introduction in a controlled manner were known by the time.

Devices operating in the range 8-14 μm spectral window as LWIR and 14-30 μm as VLWIR were made possible by the extrinsic photoconductive response of gold, copper, zinc, and mercury impurity levels in germanium. Before intrinsic detectors were developed, the extrinsic photoconductors were frequently utilized at wavelengths greater than 10 μm. However, in order to attain performance equivalent to that of intrinsic detectors, their operation at lower temperatures is required. The early 1960s saw the discovery of first extrinsic Hg-doped Ge as forward-looking IR detector, which operated in long wavelength region [20]. Ge:Hg with an activation energy of 0.09 eV was an excellent match for the LWIR range, however because the detection process relied on an external excitation, it needed a two-stage cooling mechanism to run it at 25 K. The first forward-looking IR system in actual production using Ge:Hg was constructed in 1969 for B52 Aircraft in the Air Force [21]. It produced very good imaging, but the two-stage cooling process had a short lifespan and required a lot of maintenance. In the start of 1950's, many advancements in the narrow bandgap semiconducting materials were made, which subsequently were proven to be highly sensitive together extended wavelength capabilities. InSb, a member of the III-V compound semiconductors, was the first such material. InSb attracted interest due to its narrow energy gap as well as the ease with which its single crystal can be produced using standard techniques. Moreover, the development of the semiconductor alloys of III-V ($InAs_{1-x}Sb_x$), II-VI ($Hg_{1-x}Cd_xTe$) and IV-VI ($Pb_{1-x}Sn_xTe$) material systems occurred at the end of 1950s and start of 1960s. These compositions made it possible to tune the spectral response for particular applications by manipulating the bandgap of materials. Variable band gapped alloys of $Hg_{1-x}Cd_xTe$ were first developed in 1959 by Lawson and colleagues [22]. They are practically perfect for a variety of IR detectors due to the fundamental characteristics of these narrow-gap semiconductors including the high electron mobility, high optical absorption coefficient and low thermal generation rate as well

as the ability to engineer bandgaps. Over the past 40 years, new detection technologies have been developed due to difficulties in the growth of HgCdTe, which are largely caused by the high vapour pressure of Hg. In the early 1970s and late 1960s, the PbSnTe was equally pursued [23, 24]. The growth of PbSnTe was relatively easier, and their demonstration as LWIR lasers and photodiodes is straightforward. Harman and Melngailis in 1974 [24], compared $Hg_{1-x}Cd_xTe$ and $Pb_{1-x}Sn_xTe$ systems as 'We predict that Pb_{1-x} Sn_xTe can be utilized extensively in future for detecting the blackbody radiations from 8 to 14 μm range, since the crystal growth is less expensive and more scalable for mass production. Furthermore, when compared to $Hg_{1-x}Cd_xTe$, the $Pb_{1-x}Sn_xTe$ seems to be more durable and much less degradable at high temperatures. $Hg_{1-x}Cd_xTe$, however, can be anticipated to be more advantageous in GHz frequency range for sensing heterodyne including some high-speed applications owing to its lower dielectric constant.' This perspective dramatically changed a few years later due to the chalcogenides' two major flaws. First, the high dielectric constant, which led to a high diode capacitance and consequently limiting frequency response [25]. Secondly, the extremely high thermal expansion coefficients (TEC) of IV–VI compounds [26], limiting their use for hybrid configurations with silicon multiplexers.

The advancement of material technology continuously focused on the military purposes. The Vietnam War in the US led to the development of the IR technology. When photolithography was made accessible in 1960s, the IR detector arrays were made. The linear array technology was employed for InSb, PbSe, and PbS detectors in the early stages. The first FIR forward-looking IR device was produced in 1969 by utilizing linear Ge:Hg arrays. The HgCdTe detector, in which optical transitions are related transitions from the valence band maximum (VBM) to conduction band minimum (CBM), was known at the time to be capable of achieving very good sensitivity at significantly higher temperatures, and many countries actively developed the HgCdTe based detectors [27]. In 2009, the 35th conference in Infrared Technology and Applications, which took place in Florida, scheduled a separate session for celebrating the HgCdTe's 50th anniversary. The capability of HgCdTe alloy to tune its band gap as proposed by Lawson and colleagues (in 1959) [22], has given IR detector technology a unique degree of freedom in their designs. Applications for IR detectors that cover NIR (1-3 μm), MIR (3-5 μm), long wavelength (LWIR: 8-14 μm), and FIR: 14-30 μm ranges are made possible due to its variable bandgap. The most popular variable gap semiconductor for IR photodetectors right now is HgCdTe, which successfully have gone through many challenges like lead-tin telluride and extrinsic silicon devices, although it has now more competitors. For instance the silicon-based Schottky barriers, heterojunctions of SiGe, GaInSb superlattices and AlGaAs quantum wells, high-temperature superconductors, and particularly there are two different kinds of thermal detectors (pyroelectric detectors and silicon-based bolometers). However, it is intriguing to note that none of these competed in terms of basic characteristics. However, it should be noted that the GaInSb type II superlattice could be very appealing from the physics perspective.

1.1.1 Alternatives to HgCdTe

Due to the difficulty in the synthesis of HgCdTe, particularly the high Hg vapour pressure and the solidus-liquidus separation, alternate technologies have been developed. Among them were PbSnTe [23, 24], strained $Ga_{1-x}In_xSb$ superlattices (8-14 μm range) [28], and a variety of quantum well infrared photodetectors (QWIPs) based on GaAs/AlGaAs [29-31]. InSb was found to have the narrowest energy gap as compared to other semiconductors during 1950s, that is why its use as a MIR detector was apparent. At higher working temperatures, the InSb band gap is less matched with 3-5 μm wavelength, and HgCdTe performs better. Similar to InSb in composition, the InAs has greater band gap with a threshold wavelength of 3-4 μm. The comparison of the dark currents for InSb and HgCdTe photodiodes suggests the better performance of HgCdTe based photodiodes. Due to the defect center in the energy band gap of InSb, the devices are influenced by generation-recombination currents. On other hand HgCdTe detector does not demonstrate any generation-recombination currents in the given temperature range and are instead constrained by the diffusion currents. Additionally, the HgCdTe has become the desired material because to its wavelength tunability [7]. A possible detector material for NIR range (1.0-1.7 μm) can be the alloy of $In_{0.53}Ga_{0.47}As$ with a lattice matching substrate of InP. The material can be used for applications like remote sensing, light wave communication systems, process control and the night vision due to the lower dark current and noise with respect to germanium, a competitor NIR material [32]. The photodiodes of InGaAs are shown to be of higher performance for materials with composition almost matching with InAs (cut−off wavelength of 3.6 μm) and InP (cut-off wavelength of 1.7 μm). However, the performance rapidly declines (at intermediate wavelengths) because of the defects induced by substrate lattice mismatch.

The QWIPs could be alternative hybrid detectors for the LWIR range i.e. 8-14 μm. The superlattices of GaAs/AlGaAs have been constructed to produce the high impedance detectors. The LWIR HgCdTe focal plane arrays continue to be expensive despite significant research and developments, principally due to the low yield obtained from operable arrays. The sensitivity of HgCdTe systems to defects is the cause of lower yield that occurs because of materials' fundamental properties. GaAs/AlGaAs QWIPs bear a number of benefits over HgCdTe devices, including the ability of using the standard manufacturing tools (MBE growth setup). This results in high yield and consequently lower cost with improved radiation hardness and thermal stability. Due to inherent constraints related to inter-subband transitions, LWIR QWIP cannot compete with HgCdTe photodiode as a single device, especially at higher temperatures (>70 K). The QWIP devices usually reveal low quantum efficiency and lower spectral response band. Due to many issues with HgCdTe material, for instance the Shockley-Read recombination, surface and interface instabilities, trap assisted tunneling and p-type doping, it has less distinct benefit below 50 K [30, 33].

The performance limitations for applications requiring quick integration times and the lower working temperatures are the key disadvantages of QWIP focal plane array technology. The large size focal plane arrays and the uniform performance are two key features of this technology. Due

to the widespread use of GaAs in telecommunication sector, there is a significant industrial infrastructure for the growth, packaging and processing of III-V materials and devices. Infrared detection is the only know application for HgCdTe . The lack of big size focal plane arrays required for TV format and larger formats is the major limitation in LWIR HgCdTe technology. Strain layer superlattices (SLSs) of InAs/$Ga_{1-x}In_xSb$ can be considered as one of the alternatives to HgCdTe. However, the InAs/GaInSb SLs are still in the process of development. There exist several problems including the substrate preparation, material growth, device passivation and processing. In a superlattice, the holes are located in one layer (GaInSb in this case), while electrons in the other (InAs) of the superlattice. This kind of bands alignment in the electronic structure categorizes the superlattice as type-II (see the schematic in Fig. 1.2). As a result, the carrier lifetime is increased and Auger recombination processes are suppressed. Over the last few years, InAs/In(As,Sb) Ga- and Hg free type-II superlattices (T2SLs) are widely investigated as promising candidates for IR applications due to their narrow electronic band gaps and carrier lifetimes longer compared to other systems [34-42].

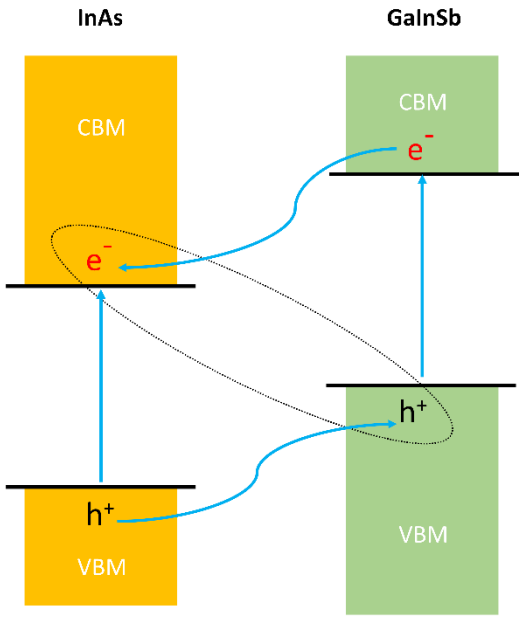

Figure 1.2 Schematic exhibiting the type-II band alignment; the electrons lie in InAs, while holes are located in GaInSb part of the superlattice.

1.2 Two-dimensional (2D) materials

The search continued on finding other materials with unique electronic and optical properties. Bulk materials just thinned to their single-layer limit may show extraordinary features due to the electron containment and their layered nature. Among these, 2D materials such as graphene and transition metal dichalcogenides (TMDs) are broadly investigated exhibiting unique electro-optical properties, which could be very promising in optoelectronic devices. There has been several

issues faced with the fabrication of the electronic devices based on bulk materials, a central drawback is their growth on flexible substrates. The discovery of 2D layered materials made it possible to design electronic devices on flexible substrates [43]. On the other side, the Moore's law scaling limit seems approaching, and thus narrowing the Si technology that is simply because of basic limitations in Si on atomic scale [44]. In view of the aforementioned drawbacks, it is intriguing to speculate about the position of 2D materials in electronics and nono-electronics.

The 2D materials has ignited the research for next generation photonic devices building the platform to different optoelectronic applications [45, 46], such as transparent electrodes [47, 48], fast photodetectors [49, 50], plasmonic devices [51], ultrafast lasers [52], and optical modulators [53]. 2D materials can be Dirac like gapless materials (graphene), insulators (hexagonal boron nitride, h-BN), semiconductors (TMDs e.g. WS_2, MoS_2 etc.), and narrow band gap materials (black phosphorus, bP) [54]. Hence, they can be found in different flavors as demonstrated in the schematic of Fig. 1.3. The most significant physical and chemical features for 2D materials are:

1) A quantum restriction that favors the 2D plane and is advantageous for the absorption of light and quantum devices.

2) Van der Waals forces, which weakly stack the atomic planes on top of one another making it easier to build heterostructures and providing the possibility to integrate these layered structures with silicon chips.

3) Nanodevices devoid of parasitic capacitance can be produced with atomically thin 2D materials.

4) Devices with extraordinary performance could be made possible due to the absence of dangling bonds at the surfaces and interfaces of layered structures.

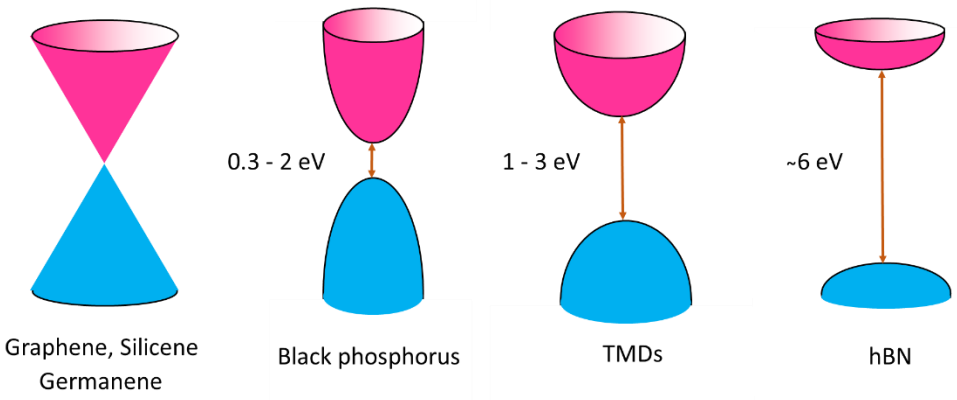

Figure 1.3 Illustration of bandgaps for different 2D materials. The true value of the bandgap is dependent on a number of factors such as the number of layers, chemical doping and strain level.

Since graphene has no gaps, there is a large dark current that significantly lowers photodetection's sensitivity and prevents future advancement in optoelectronics. The discovery and novel tools of growing 2D materials bearing direct energy band gaps that are tunable from visible region to IR spectral window have given an insight of manufacturing the photodetectors. Nicolosi et al. grouped the different 2D materials covering a wide spectral range of the optoelectronic properties as: atomically thin h-BN (UV region), TMDs (visible to IR), bP (layer dependent band gaps from visible to IR), metal halides (PbI_2, $MgBr_2$), metal oxides (MnO_2, MnO_3), and halide perovskites [55]. 2D TMDs have chemical formula as MX_2, where M represents transition metal (such as Mo, Hf, W, Nb, Re, etc.) while X stands for chalcogen atom (like Te, Se, S) [56]. The pair of X layers sandwich a single layer of M atoms. There are three polytypes of layered TMDs: 1T (trigonal), 2H (hexagonal), and 3R (rhombohedral), each of which has a unique set of electrical characteristics ranging from metallic to semiconducting and/or even superconducting [57]. Unlike graphene, whose electronic properties depends on the hybridization of 's' and 'p' orbitals, the electronic attributes of TMDs instead are dependent on the coordination environment and filling of 'd' orbitals of transition metal element. From group IV to X in periodic table, in a transition metal the d electrons varies from zero to six, correspondingly. A semiconducting behavior results from the fully filled d orbitals (2H-MoS_2 of group VI and 1T-PtS_2 of group X), whereas metallic nature is observed for the partially filled d states (2H-$NbSe_2$ of group V and 1T-ReS_2 from group VII). The electro-optical characteristics of TMDs are thickness dependent, i.e. on the number of layers and differ greatly from those of their bulk counterpart. Bulk materials of TMDs are known to be indirect band gap semiconductors with typical 1 eV bandgap. The band structure switches from a narrow indirect nature to a wide direct, as the bulk is thinned to monolayer. As a result, TMDs are able to detect light at various energies thereby modulating the electronic bandgap via changing the layers of TMDs. These variations in the optoelectronic properties occur due to the surface and quantum confinement effects [46, 50, 58-61]. Furthermore, the application of strain can also have a significant impact on the materials' optical and electrical characteristics [62, 63].

The optical absorption taking place in the spectral range from visible to near-infrared is mostly caused by the electron direct transition from valence to conduction band at K/K' points in 2D Brillouin zone. This explains why TMDs have absorption coefficient in the range 10^4-10^6 cm^{-1}, which is comparatively higher. Consequently, TMD films having sub-micron thickness absorb more than 95 % of electromagnetic radiations coming from the sun. TMDs, such as MoS_2, $MoSe_2$, and WS_2 demonstrate even better absorbance in the UV to NIR region than graphene. The region of absorbance can be broadened to MWIR region due to defect or edge states in the electronic band gap and comparatively higher ratio of edge-to-surface area [63]. It is necessary to use the layered semiconductors with low bandgaps and high mobilities for LWIR detector devices. The group-X noble TMDs, which have recently been revisited with broadly tweakable bandgaps, anisotropy, air stability, and moderate carrier mobility [64], offer such a possibility. Theoretically, the bandgaps for the bilayers and bulks of this class (PtX_2, where X=Se, S) might be as low as 0-0.25 eV, and the carrier mobility is found to be above 1000 cm^2/Vs at ambient temperature [65, 66]. TMD monolayers are regarded as promising materials for optoelectronics and could be ideal as the

channel layered materials FETs due to their inherent band gap of 1.1–1.9 eV [67-71]. Furthermore, the spin splitting in the range 150-500 meV at the corners (K, K' points) of the hexagonal Brillouin zone is caused by inversion symmetry breaking combined with spin-orbit interaction causing from the metal atoms' d orbitals of TMD monolayers [72-75]. TMDs are considered as typical valleytronic materials due to the strong coupling among the spin and valley degrees of freedom [76-78].

1.2.1 Hybrid 2D materials

The 2D TMDs due to their unique crystal structures and extraordinary physical properties are the materials of choice in applications such as electronics, photonics, valleytronics and optoelectronics [79-82]. However, integrating the 2D materials with other layered structures in the form of heterostructures and/or superlattices could be very promising. In particular, the 2D TMDs could be skillfully bring-together thereby fabricating various heterostructures or superlattices possessing exotic features, which cannot be acquired from the isolated component of the layered 2D material, thus providing the opportunities to explore and investigate the novel applications for the nanodevices [83-85]. In nanoelectronics and optoelectronics, the hybrid structures between different 2D materials could be very crucial building blocks because of their versatility and greater capacity [62, 86-90]. The mechanical exfoliation followed by the pick-up-and-transfer technique can be used to create 2D layered heterostructures, but chemical vapor deposition (CVD) enables the direct growth of TMDs layers that are lattice aligned for both the heterostructures i.e. Van der Waals vertical heterostructures and lateral heterostructures having sharp interfaces. Moreover, the monolayer TMD on a wide scale can be synthesized on large scale with seeding promoter-assisted-CVD. Based on the choice of seeding promoter and its capacity to adhere to substrates, this strategy was subsequently adapted for the construction of a range of vertical and lateral hybrid-structures. Besides, it is demonstrated that the technique is independent of lattice mismatch among the combining materials (2D and TMD) to create vertical or lateral heterostructures [91-93]. One-step or two-step CVD synthesis have both been used to effectively produce a number of lateral heterostructures, including MoS_2/WSe_2, NbS_2/MoS_2, $MoS_2/MoSe_2$, and $ReS_2/ReSe_2$, MoS_2/WS_2 (the top and side views for such structure are shown in Fig. 1.4b).

The laterally stitched and van der Waals heterostructures demonstrate abrupt change in their optoelectronic features due to their unique quality of interfaces and their distinctive electrostatics, and thus such heterostructures between the various 2D materials have recently attracted a lot of interest [92, 94-97]. The heterostructures of 2D materials are superior to bulk hetero-systems in that they have larger depletion region, and therefore are more sensitive to charge fluctuation [98, 99], making them perfect for optoelectronic applications [100, 101].

1.2.2 Janus structures

2D transition metal chalcogenides structures have undergone substantial research and found a wide range of uses in electronics and optoelectronics [70, 102-104]. The TMDs bearing the bandgaps

in the range of 1.1–1.9 eV with promising mechanical and electronic properties make them suitable to use these systems in photonics and electronic devices [69, 76, 105, 106]. At the corners of the hexagonal Brillouin zone of TMDs, there exist high spin splitting due to the absence of inversion symmetry, and significant spin-orbit coupling (SOC), which is produced by the d-orbitals of transition metals in TMDs [73-75]. Because of the strong correlation between the spin and valley degrees of freedom, the TMDs are regarded as the optimal materials in valleytronics [76-78]. Additionally, the alloy composition in TMDs, such as in $Mo_xW_{1-x}S_2$, MoS_xSe_{2-x}, and MoS_xSe_{2-x}, might be used to modify the electrical and optical characteristics [107-111]. Recently, the CVD approach has been used to successfully develop the Janus phase of MoSSe in the 2H phase [112, 113], where the S layer is replaced with Se atoms in the case of MoS_2, while the Se layer with S atoms in $MoSe_2$. In contrast to MX_2 (M=Mo, W, and X=S, Se), which has mirror symmetry, the Janus structure i.e. MXY (M=W, Mo, X=Se, S, and Y=S, Se) displays the out-of-plane piezoelectricity and Rashba-type spin splitting due to the perpendicular electric field that results from the breaking of mirror symmetry [72, 114-116]. Figure 1.4c shows the structures for pure and Janus phases of TMDs.

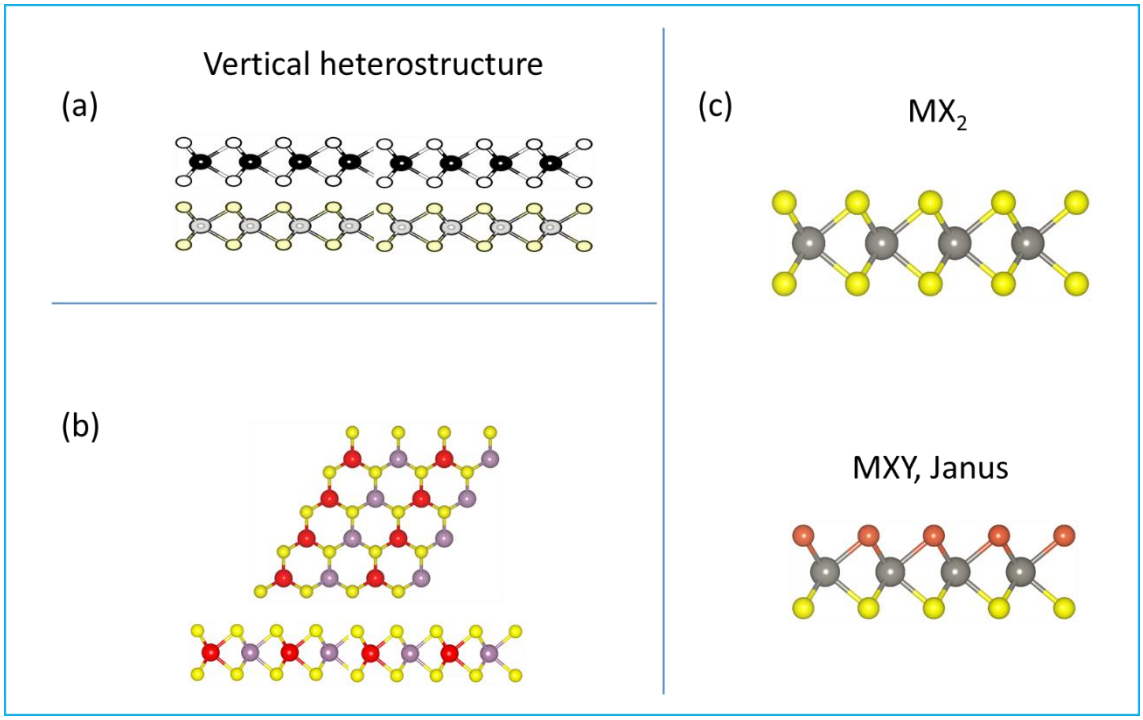

Figure 1.4 (a) Side view of vertically stacked heterostructure (b) Top and side views of parallel stitched 2D superlattice of MX_2 class, (c) representation of pristine (MX_2) and Janus structure (MXY).

1.3 MA_2Z_4 2D materials

Recently, a novel class of 2D materials MA_2Z_4, (where M represents a transition metal, A stands for group IV element, while Z is group V element) has received considerable attention owing to their exceptional properties [117]. The $MoSi_2N_4$ is first 2D material of this group, which was successfully grown using the CVD method over a big surface of 15 mm by 15 mm. This septuple-atomic-layer semiconducting material (N-Si-N-Mo-N-Si-N) may be viewed of as the three atom thick MoN_2 sandwiched between the two SiN layers with indirect band gap of about 1.94 eV. The elastic modulus of a monolayer of $MoSi_2N_4$ is about four times greater than that of a single layer of MoS_2, and the carrier mobilities of holes and electrons are correspondingly four to six times greater. Moreover, calculations using density functional theory predict the existence of a novel family called MA_2Z_4 (M is Transition metal, A is IV-element, and Z is V-element). The extraordinary attributes of this family have been the subject of several studies to date [118-125].

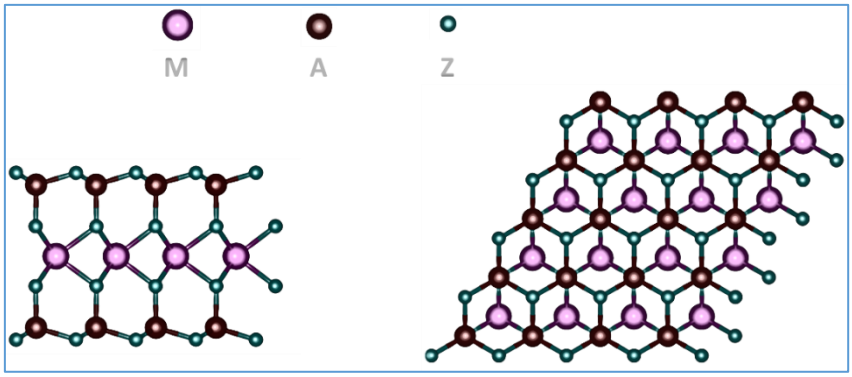

Figure 1.5 Side and top view of MA_2Z_4 family of 2D materials.

1.3 Thesis Outline

Using density functional theory (DFT), this thesis aims to address the electronic and optical properties of 3D InAs/$InAs_{0.625}Sb_{0.375}$ superlattice, XSi_2N_4 (Mo, W, Ti) 2D materials and their heterostructures $MoSi_2N_4/XSi_2N_4$ (W, Ti), and the pristine $MoSi_2P_4$ and Janus structures $XGeSiP_2As_2$ (X = Mo, W).

Chapter 2 is devoted to methodologies and computational details. First, the density functional theory is introduced, discuss different exchange–correlation functionals and the limitations of DFT. Then we review the nuts and bolts of DFT.

In **Chapter 3**, we give a brief overview of the main results compiled in this thesis along with the summaries of the papers attached. This thesis is the collection of four papers attached in this chapter. In paper I, the electronic and optical properties of the bulk InAs and InSb using modified Becke-Johnson (MBJ) exchange-correlation functional together with generalized gradient

approximation (GGA) for the exchange-correlation potential are discussed. After the validation of our approach, we studied the InAs/$InAs_{0.625}Sb_{0.375}$ SLs with three lattice constants of bulk InAs, GaSb and AlSb, respectively. In paper II, the structural stability and electronic properties of the monolayers of 2D materials such as $MoSi_2N_4$, WSi_2N_4, and $TiSi_2N_4$, and that of 2D heterostructures like $MoSi_2N_4/WSi_2N_4$, and $MoSi_2N_4/TiSi_2N_4$ are investigated. In paper III, the study is extended for the laterally stitched heterostructures, where the tuning of the electro-optical attributes via biaxial strain engineering is addressed. In paper IV, the electronic, spintronic and optical properties of pristine $MoSi_2P_4$ and Janus structures $XGeSiP_2As_2$ (X = Mo, W) for this new class of 2D materials are reported.

Finally, the last **Chapter 4** is dedicated to the conclusions.

Chapter 2

METHODOLOGY AND COMPUTATIONAL DETAILS

2.1 Many body electron system

Consider a scenario where you need to describe the properties of a clearly defined group of atoms, such as the atoms that make up a single molecule or the crystal structure of an intriguing material. The precise properties of a material can be approximated by taking into account every possible interaction, such as electron-electron, electron-nucleus, and nucleus-nucleus interactions. The following is a description of the Hamiltonian of a material with many-body interactions;

$$\hat{H} = \hat{T}_n + \hat{T}_e + \hat{V}_{n-n} + \hat{V}_{e-e} + \hat{V}_{n-e} \tag{2.1}$$

Where $\hat{T}_n$, $\hat{T}_e$ represent the system's nuclei and electrons' kinetic energies.

$$\hat{T}_n = \sum_{\alpha=1}^{K} \frac{(-i\hbar\nabla_{R\alpha})^2}{2M_\alpha}$$

$$\hat{T}_e = \sum_{\alpha=1}^{N} \frac{(-i\hbar\nabla_i)^2}{2m}$$

Here m is the mass of the electron in the N electron system and $R\alpha$ is the Cartesian coordinate of the nucleus with mass $M\alpha$. There are two types of Coulomb interactions that exist among the particles indicated in Eq. 2.1; the $\hat{V}_{n-e}$ potential which is between a nucleus and an electron (attraction), and $\hat{V}_{n-n}, \hat{V}_{e-e}$ represent the Coulomb repulsion potentials between the nuclei and electrons, respectively.

$$\hat{V}_{n-n} = \sum_{\alpha,\beta=1;\alpha<\beta}^{K} \frac{Z_\alpha Z_\beta e^2}{|\vec{R}_\alpha - \vec{R}_\beta|}$$

$$\hat{V}_{e-e} = \sum_{i,j=1;i<j}^{N} \frac{e^2}{|\vec{r}_i - \vec{r}_j|}$$

$$\hat{V}_{n-e} = -\sum_{\alpha=1}^{K}\sum_{i=1}^{N} \frac{Z_\alpha e^2}{|\vec{R}_\alpha - \vec{r}_i|}$$

where the i^{th} and j^{th} electrons are indicated by the letters r_i and r_j. A many-electron system's Hamiltonian may be expressed as

$$\hat{H} = \sum_{\alpha=1}^{K} \frac{(-i\hbar\nabla_{R\alpha})^2}{2M_\alpha} + \sum_{\alpha=1}^{N} \frac{(-i\hbar\nabla_i)^2}{2m} + \sum_{\alpha,\beta=1;\alpha<\beta}^{K} \frac{Z_\alpha Z_\beta e^2}{|\vec{R}_\alpha - \vec{R}_\beta|} + \sum_{i,j=1;i<j}^{N} \frac{e^2}{|\vec{r}_i - \vec{r}_j|}$$

$$- \sum_{\alpha=1}^{K}\sum_{i=1}^{N} \frac{Z_\alpha e^2}{|\vec{R}_\alpha - \vec{r}_i|} \qquad (2.2)$$

One may solve the time-independent Schrödinger equation to determine the electronic characteristics of a many-electron system by taking into account all of the Hamiltonian's terms in Eq. 2.2.

$$\hat{H}\Psi = E\Psi \qquad (2.3)$$

'Ψ' represents the eigenstates or a set of solutions of the Hamiltonian with the associate eigenvalues Ethat is a real quantity. Since there are 10^{23} times more ions and electrons in actual systems, it is challenging to find a precise solution to the equation with current computational resources. Approximations are necessary to solve this problem.

We must determine the locations of both the electrons and nuclei in order to find the location of an atom. Atomic nuclei are significantly heavier than individual electrons; in a nucleus each proton or neutron is more than 1800 times heavier than the mass of an electron. This is an important finding for applying quantum mechanics to atoms, which basically indicates that electrons react to changes in their environment considerably faster than those of nuclei. Thus, we can divide our physical query into two parts. First, the equations describing the many electron system are solved for fixed locations of the atomic nuclei. We determine the lowest energy configuration, or state, of the electrons for a specific set of electrons travelling in the field of a particular set of nuclei. This lowest or minimum energy configuration is termed as the ground state of system, and the formalism that separates the nuclei and electrons in the separate mathematical schemes is known as the Born Oppenheimer approximation. The Born Oppenheimer approximation, the first and most significant approximation, allows one to separate the motion of the electrons and ions, because in a typical solid ions travel far more slowly than electrons do. This approach assumes that the potential energy of ions is constant and the kinetic energy of ions is ignored. Hamiltonian therefore becomes;

$$\hat{H} = \sum_{i=1}^{N} \frac{(-i\hbar\nabla_i)^2}{2m} + \sum_{i,j=1;i<j}^{N} \frac{e^2}{|\vec{r}_i - \vec{r}_j|} - \sum_{\alpha=1}^{K}\sum_{i=1}^{N} \frac{Z_\alpha e^2}{|\vec{R}_\alpha - \vec{r}_i|} \quad (2.4)$$

This approximation allows us to decouple the wave function that may be expressed as the product of the ionic and electronic wave functions i.e.

$$\Psi = \Psi_{ik}^{n}(\vec{R}_\alpha)\, \Psi_k^e(\vec{r}_i\,,\ \vec{R}_\alpha) \quad (2.5)$$

The details of Hamiltonian are dependent on the state and situation of the physical system that the Schrödinger equation describes. There are several well-known instances where the Hamiltonian has a simple form and the Schrödinger equation can precisely be solved, such as particle in a box problem and that of harmonic oscillator. The problem we are dealing with is a more complex scenario when several electrons are interacting with numerous nuclei. Therefore, the Schrödinger eq. by taking into account the Born-Oppenheimer approximation is expressed as;

$$[\hat{T}_e + \hat{V}_{e-e} + \hat{V}_{n-e}]\, \Psi_k^e(\vec{r}_i\,,\ \vec{R}_\alpha) = E_k\ (R - \alpha)\, \Psi_k^e(\vec{r}_i\,,\ \vec{R}_\alpha) \quad (2.6)$$

For a set of frozen ions situated at $\vec{R}_\alpha$, the eigenvalue problem represented by Eq. 2.6 is stationary. Solving Eq. 2.6 is a difficult task due to many reasons, for instance, (i) the many meta-stable state arrangements for nuclei, (ii) intricate geometry of many body (many electrons) systems, and (iii) the enormous number of the electrons and their quantum nature. Therefore, even if the ion mobility is neglected, a more effective approximation is required to solve this problem. For that reason, we now discuss Hartree-Fock (HF) formalism, which is also called self consistent field approximation. In this approach, the ground state for a many electron system Ψ_0^e is exemplified by the product of single particle states termed as Slater determinants.

$$\Psi_0^e(\vec{r}_i\ \sigma_1,\ldots\ldots \vec{r}_N\ \sigma_N) \approx \phi_{1\ldots\ldots N}\ (\vec{r}_i\ \sigma_1,\ldots\ldots \vec{r}_N\ \sigma_N) \quad (2.7)$$

Where, ϕ_i stand for single electron wave functions with the spins denoted as σ_i, and the $\phi_{1\ldots N}$ representing the ground state wave of functions are obtained using the variational principle. One can notice that the HF scheme is analogous to the usual Schrödinger eq., where the effective potential shows a non local nature through the terms $V_H(r)$ (Hartree Coulomb potential) and V_x^{HF} (the exchange potential).

$$\left[\frac{(-i\hbar\nabla_i)^2}{2m} + V_H(r) + V_x^{HF}\right]\phi_i(\vec{r},\sigma) = E_i\phi_i(\vec{r},\sigma) \quad (2.8)$$

While $V_H(r)$ and V_x^{HF} are given as;

$$V_H(r) = \int \frac{d^3r'}{|\vec{r} - \vec{r}'|} \sum_{\sigma'=\uparrow,\downarrow} \sum_{j\neq i} \left|\phi_j\left(\vec{r}', \sigma'\right)\right|^2$$

$$V_x^{HF}(\vec{r}\sigma,\vec{r}'\sigma') = \frac{e^2}{|\vec{r}-\vec{r}'|}\sum_{j=1}^{N}\phi_j(\vec{r}\sigma)\phi^*{}_j(\vec{r}'\sigma')$$

The potentials are calculated self consistently; it starts with an initial guess, the potential and the ϕ_i states are improved step by step. Once a certain level of precision is attained, the iterative procedure is terminated. In the HF approach the electron-electron Coulomb repulsions are not taken into account and the wavefunction of N-electrons is approximated by the average field of the whole electron cloud. In order to take into account the Coulomb repulsion, the unoccupied states (finite or infinite) must be included together with the occupied states. The improved correlated wave function is given by;

$$\Psi_k(\vec{r}_1\,\sigma_1,\ldots\ldots\,\vec{r}_N\,\sigma_N) = \sum_{i_1\ldots\ldots i_N} C^k_{i_1\ldots\ldots i_N}\;\; \phi_{i_1\ldots\ldots i_N}\,(\vec{r}_1\,\sigma_1,\ldots\ldots\,\vec{r}_N\,\sigma_N) \qquad (2.9)$$

The expansion coefficient is calculated in a number of ways. The single electron wave functions $\phi_{i_1\ldots\ldots i_N}$ should be expanded in a finite set of basis functions for efficient numerical implementations.

$$\phi_i(\vec{r}\sigma) = \sum_{k=1}^{M} b_{i,k\sigma}\,\eta_k(\vec{r}) \qquad (2.10)$$

With the matrix elements $<\eta_k|\eta_l>$, Eq. (2.8) becomes an eigenvalue problem, the $b_{i,k\sigma}$ are determined simultaneously. Thus using the HF method, an effective single particle formalism is written as;

$$\sum_{l=1}^{M}\sum_{\sigma'}\left[\langle\,\eta_k\left|-\frac{(-i\hbar\nabla_i)^2}{2m}\delta_{\sigma,\sigma'}+v_{eff}\,\sigma,\sigma'\right|\eta_l\rangle-\;\epsilon_i\langle\,\eta_k|\eta_l\rangle\right]b_{i,l\sigma'}=0 \qquad (2.11)$$

Here, the potential experienced by the electrons is $v_{eff}\,\sigma,\sigma'$.

There are always searches for alternative approaches that can fully map the interactive many-body problem onto an effective single particle problem. Such an approach should include the correlations in some fashion to make it applicable for approximating the properties of a system precisely. One such scheme is the density functional theory (DFT), which is a remarkable method, which simply replaces the wave function concept with the electron density (ρ).

2.2 Density functional theory (DFT)

The fundamental concept of Density functional theory is the electronic density (ρ) that replaces the idea of wave function representing the many-body arrangement. As a result, the number of

scaling factors in the numerical algorithm is reduced. The ground state electronic density can be expressed as;

$$\rho(\vec{r}) = \langle \Psi_0 | \hat{\rho}(\vec{r}) | \Psi_0 \rangle$$

$$= N \sum_{\sigma_1, \ldots\ldots \sigma_N} \int d^3 r_2 \ldots\ldots d^3 r_N \, |(\vec{r}_1 \, \sigma_1, \ldots \ldots \vec{r}_N \, \sigma_N)| \Psi_0 >|^2 \qquad (2.12)$$

Two key mathematical theorems established by Kohn and Hohenberg, as well as a series of equations derived by Kohn and Sham in the mid-1960s, provide the foundation of the whole area of density functional theory. The first theorem is that '*the ground-state energy derived from Schrödinger's equation is a unique functional of the electron density, i.e. E=E[ρ(r)]*' as demonstrated by Hohenberg and Kohn, with ρ(r) as the electron density. This is the reason why this discipline is called density functional theory. This theorem can also be stated as *'The ground-state electron density is the only determinant of all ground-state features, including the energy and wave function, according to Hohenberg and Kohn.'*An essential characteristic of the functional is defined by the second Hohenberg-Kohn theorem: *'The actual electron density corresponding to the complete solution of the Schrödinger equation is the one that minimizes the energy of the overall functional.'*

2.2.1 Kohn-Sham equations

Unfortunately, the Hohenberg-Kohn (HK) theorem does not define the exact form of E[ρ(r)]. An accurate mapping of the interacting N-particle problem onto an effective non-interacting system can simplify the problem in question, which is feasible within the Kohn-Sham (KS) formalism. The single particle orbitals in the KS-scheme are referred to as KS orbitals ($\Psi_i^{\mathrm{KS}}(\vec{r})$), which mimic the density of the real system.

$$\rho(\vec{r}) = \sum_{i=1}^{N} \left| \Psi_i^{\mathrm{KS}}(\vec{r}) \right|^2 \qquad (2.13)$$

$\Psi_i^{\mathrm{KS}}(\vec{r})$ follow the KS eq.

$$\left[-\frac{(-i\hbar\nabla_i)^2}{2m} \delta_{\sigma,\sigma'} + V_{eff}^{[\rho]}(\vec{r}) \right] \Psi_i^{\mathrm{KS}}(\vec{r}) = \mathrm{E}_i \Psi_i^{\mathrm{KS}}(\vec{r}) \qquad (2.14)$$

Here, $V_{eff}^{[\rho]}(\vec{r})$ is the effective potential that is function of density 'ρ' of electrons and E_i denote the KS eigenvalues. The $V_{eff}^{[\rho]}(\vec{r})$ is rewritten as;

$$V_{eff}^{[\rho]}(\vec{r}) = V_{ext}^{[\rho]}(\vec{r}) + V_H^{[\rho]}(\vec{r}) + V_{XC}^{[\rho]}(\vec{r}) \qquad (2.15)$$

$V_{ext}^{[\rho]}(\vec{r})$ represent the external potential which is given as;

$$V_{ext}^{[\rho]}(\vec{r}) = \int d^3r v_{ext}\,\rho(\vec{r}) \tag{2.16}$$

$V_H^{[\rho]}(\vec{r})$ is the density-dependent classical (Hartree) interaction between the N particles

$$V_H^{[\rho]}(\vec{r}) = \frac{1}{2}\int d^3r \int d^3r' \frac{\rho(\vec{r})\,\rho(\vec{r}')}{|\vec{r}-\vec{r}'|} \tag{2.17}$$

$V_{XC}^{[\rho]}(\vec{r})$ stands for the exchange–correlation functional, that includes all quantum mechanical effects.

$$V_{XC}^{[\rho]}(\vec{r}) = \frac{\delta E_{XC}[\rho]}{\delta\rho(\vec{r})} \tag{2.18}$$

Here, $E_{XC}[\rho]$ stands for the exchange-correlation functional of total energy, which takes into account all possible interactions of many-body problem. Although the precise form of $E_{XC}[\rho]$ is not known, since it depends on electron density, it might be reliably predicted self consistently. If the precise form of $V_{XC}^{[\rho]}(\vec{r})$ is calculated, the Kohn-Sham equation can calculate the exact ground state energy. It is difficult to determine and computationally expensive to compute the precise shape of the exchange-correlation term of a many electron system. In the following, we discuss some approaches of approximation for $E_{XC}[\rho]$.

In general, the exchange correlation potential $E_{XC}[\rho]$ is composed of two contributions; one is the Exchange part $E_C[\rho]$, and the other is the correlation part $E_X[\rho]$ in the many-body problem. There are different approximation functionals to calculate $E_{XC}[\rho]$, two of these are well-known approximations known as the local density approximation (LDA), and the other is called general gradient approximation (GGA).

2.2.2 Local density approximation (LDA)

The Hohenberg-Kohn theorem guarantees the existence of exchange-correlation functionals, but it is simply unknown what their exact form is. Fortunately, the uniform electron gas is one instance where this functional can precisely be deduced. In this case, the electron density is ρ(r) is constant in the whole space. Since the variation in electron density ρ(r) form chemical bonds and in general make materials interesting, this scenario could seem to be of little relevance in any actual material. However, the uniform electron gas offers a useful application for the Kohn-Sham equations. To do this, we set the known exchange-correlation potential at each point to equal the electron density measured at that position of the uniform electron gas. This approximation is known as the local density approximation (LDA) because it only employs the local density to approximate the exchange-correlation functional. LDA is the foundation of all exchange correlation functionals. The electron gas is supposed to have a slowly fluctuating density. Subsequently, the exchange correlation energy remain locally uniform at small volume d^3r. Then, the $E_{XC}[\rho]$ within the LDA formalism is given as;

$$E_{XC}[\rho] = \int \rho(\vec{r})\epsilon_{XC}[\rho(\vec{r})]d^3r \quad (2.19)$$

Where $E_{XC}[\rho]$ denotes the exchange relation energy for the density ρ(r) of uniform electron gas.

2.2.3 Generalized gradient approximation (GGA)

A generalized gradient approximation is considered to be the best-known functional after LDA, which not only makes use of the information of the local electron density, but also considers the local gradient in the electron density. It is easy to assume that the GGA must be more accurate because it contains more physical data than the LDA. There are several diverse GGA functionals due to the numerous ways in which information from the gradient of the density ρ(r) may be included. The Perdew-Wang functional (PW91) and the Perdew-Burke-Ernzerhof (PBE) functional are two of the most often employed functionals in DFT involving solids. These functions are all GGA functions. In our calculations, we used the PBE approach in the framework of GGA to treat electron exchange–correlations [126, 127]. When GGA is applied to systems with homogenous electron densities, this approximation performs rather well and produces comparatively better results for the metals. Unfortunately, it significantly underestimates the band gap in semiconductors. When compared to LDA, the GGA approximation takes into consideration the first order correction of the electron density ρ(r). Consequently, it includes the impact of the electron density's local inhomogeneity. Using GGA, the total exchange correlation energy can be expressed as:

$$E_{XC}[\rho(\vec{r})] = \int \rho(\vec{r})\epsilon_{XC}[\rho(\vec{r}), \nabla\rho(\vec{r})]d^3r \quad (2.20)$$

2.2.4 Other exchange-correlation functionals

DFT employs a number of techniques to help with band gap issues and the materials' electronic structure, including the LDA+U, GGA+U scheme, meta-GGA functional scheme, van der Waals correction (vdW) strategy, different hybrid functional like HSE, and GW. In this this, we utilized the GGA, MBJGGA, and HSE functionals for the computations in 3D, 2D superlattices and Janus structures. The most common approach to employing a plane-wave basis set to solve the Kohn-Sham equation with the pseudopotential is described in the next section.

2.2.5 Plane wave basis set

In this thesis, we will emphasize in applying DFT to materials that are periodic in space (e.g. crystalline materials). We used the lattice vectors a_1, a_2, and a_3 to determine the geometry of the supercell, a cell that repeats itself repeatedly in space. The solution of the Schrödinger equation for a periodic system should satisfy the Bloch's theorem, a basic requirement. This follows;

$$\Psi_{ik}(\vec{r}) = e^{\vec{k}.\vec{r}}\, u_{ik}(\vec{r}), \qquad u_{ik}(\vec{r} + \vec{R}) = u_{ik}(\vec{r}) \quad (2.21)$$

where $u_{ik}(\vec{r})$ exhibits the same periodicity as the supercell in space, with the lattice vector $\vec{R}$. According to this theorem, it is conceivable to attempt to independently solve the Schrödinger equation for each value of k. This conclusion is valid for quantities that are derived from the solutions of Schrödinger equation, such as the electron density. As a consequence, solving the mathematical problems raised by DFT in k-space (momentum space) is often far more practical than solving them in real space. Calculations based on this concept are usually referred to as 'plane-wave calculations' since the functions $e^{\vec{k}.\vec{r}}$ represent plane waves. In a plane wave basis set with a periodic condition, the Bloch wave function $\Psi_{ik}(\vec{r})$ may be expanded as;

$$\Psi_{ik}(\vec{r}) = \sum_{G} C_{i,k}^{\vec{G}} e^{i(\vec{k}+\vec{G})} \tag{2.22}$$

In this case, $C_{i,k}^{\vec{G}}$ is the expansion coefficient, and G is the reciprocal lattice vector. To increase computing efficiency, the sum should be limited to an ideal number of plane waves rather of the infinite number that exists in reality. With origin at the center, all the G vectors in a sphere with a radius of $\left|\vec{G}_{max}\right|$ are considered. The following eq. is used to determine the $\left|\vec{G}_{max}\right|$ from the kinetic energy cut off (E_{cut}).

$$E_{cut} = \frac{\hbar^2\left|\vec{k}+\vec{G}_{max}\right|^2}{2m} \tag{2.23}$$

2.2.6 Pseudopotential

The orthogonality requirement between the valence electron wave function and the core electron wave function must be satisfied. Because of the rapid oscillations of wavefunction closer to the core of atoms, the energy scale spanned by the core electrons differs significantly from that of the valence electrons. As a result, Eq. requires a high number of plane waves to accurately characterize the valence electron wave function. However, the characteristics of solids are not significantly influenced by the core electrons. Because of this, an effective method known as the pseudopotential approach can be used in place of the real potential. Chemical bonding and other physical properties of materials are mostly determined by the less firmly coupled valence electrons; core electrons are not very significant in determining these properties. It was obvious from the first plane-wave procedure that calculations which mimicked the characteristics of core electrons in a way might decrease the number of plane waves necessary in a calculation may have considerable advantages. The usage of pseudopotentials is the most crucial strategy for lowering the computational burden caused by core electrons. Conceptually, a pseudopotential substitutes a smoothed density chosen to correspond to several significant physical and mathematical characteristics of the real ion core for the electron density from a selected set of core electrons. One such approach is the projector augmented-wave (PAW) method that was first introduced by Blöchl, later remodeled for plane-wave calculations by Joubert and Kresse. Materials possessing large electronegativity differences and strong magnetic moments, the PAW formalism is found to

be more reliable compared to other approaches. In this thesis, all the calculations are performed using PAW method that is built-in to VASP code.

Let's assume that the Kohn-Sham equation is satisfied by the system's real wave function;

$$\left[-\frac{(\hbar\nabla_i)^2}{2m} + V_{eff}^{[\rho]}(\vec{r})\right] \Psi_i^{KS}(\vec{r}) = E_i \Psi_i^{KS}(\vec{r}) \tag{2.24}$$

A pseudo wave function may be constructed as;

$$\Psi_i^{KS}(\vec{r}) = (1 - \hat{P})\phi_i(\vec{r}) \tag{2.25}$$

where the $\hat{P}$ signifies the projection operation that is expressed as follows;

$$\hat{P} = \sum_j |k_j><k_j| \tag{2.26}$$

Any function can be projected by the $\hat{P}$ here to the core states ($|k_j>$). It may be demonstrated that $\Psi_i(r)$ can satisfy the equation as $\Psi_i^{KS}(r)$.

$$\left[-\frac{(\hbar\nabla_i)^2}{2m} + V_{ps}(\hat{r})\right] \phi_i(\hat{r}) = E_i \phi_i(\hat{r}) \tag{2.27}$$

Here, $V_{ps}(\hat{r})$ is the pseudopotential and it can be expressed as;

$$V_{ps}(\hat{r}) = V_{eff}^{[\rho]}(\vec{r}) - \left[-\frac{(\hbar\nabla_i)^2}{2m} + V_{eff}^{[\rho]}(\vec{r})\right]\hat{P} + E_i\hat{P} \tag{2.28}$$

Chapter 3

PAPERS COMPRISING THE THESIS

3.1 A short overview of the main results

Dimensionality of materials have revealed important impacts on their attributes. In addition to referring to the materials' structural characteristics, this also affects many of their electronic and optical properties [128]. To this end, we first investigate the electronic and optical features of InAs and InSb bulk, and then those of InAs/$InAs_{0.625}Sb_{0.375}$ 3D superlattice via first principles approach. We observed that the electronic and optical properties are modified remarkably in the superlattice geometry. A strong dependence of the electronic and optical features on the variation of lattice constant is observed. A considerable decrease in the effective masses for heavy-holes and energy gaps in the k_x-k_y plane is noticed as compare to their bulk phases of the parent compounds. The absorption spectra in the far-infrared regime is strongly increased in the case of superlattice with respect to bulk InAs and InSb suggesting their applications in the long-wavelength IR detectors. Moreover, a great deal of interest in 2D materials has been sparked by the successful "isolation" of graphene from the bulk graphite and the findings of its extraordinary physical features, such as ultrahigh electron mobility, ballistic carrier transport, and anomalous quantum Hall effect [129, 130]. Here, inspired from the excellent features of the newly discovered 2D materials family MA_2Z_4, we explore the monolayers XSi_2N_4 (X = Mo, W, and Ti) and the vertical and lateral heterostructures of these structures including $MoSi_2N_4$/WSi_2N_4, and $MoSi_2N_4$/$TiSi_2N_4$. After establishing the thermodynamical stability of both, the monolayers and heterostructures, we studied the electronic band structures and the density of states indicating a semiconducting behavior with the band gaps ranging from 0.30 to 2.60 eV giving the possibility to utilize them for photovoltaics and other photonic devices operating in the visible range (IR detectors). Besides, we investigated the effect of biaxial strain on the electro-optical properties of laterally stitched heterostructures, which revealed significant modifications in the electronic band structures and optical spectra. Lastly, the pristine $MoSi_2P_4$ and Janus phase such as $XGeSiP_2As_2$ (X = Mo, W) are studied in detail presenting outstanding thermodynamical stabilities. Comparing to pristine $MoSi_2P_4$, the Janus structures $XGeSiP_2As_2$ (X = Mo, W) possessing broken mirror symmetry indicate small direct band gaps, larger spin splittings at K/K’ and the Rashba spin-splitting. The

large spin and Rashba-type splittings together with the exceptional electronic and optical features in the Janus structures can make extraordinary contribution in the valleytronics, spintronics and IR applications.

3.2 PAPER I: InAs/$InAs_{0.625}Sb_{0.375}$ 3D Superlattice

Owing to the small band gaps and longer carrier lifetime, the Ga- and Hg-free type-II superlattices (T2SLs) of InAs/(InAsSb) have gained attention as viable options for infrared detector applications during the past several years [7, 34, 36-39, 41, 131]. Besides, the In(As,Sb) based quantum wells and their nanowires are suggested as a platform to observe the topological superconductivity [132], whereas the InAs/GaSb heterostructures due to their type-III band bending have been reported to host topological states [133-135]. Generally, electronic band structures for III-V semiconductors are investigated within the tight-binding approximation or using the envelope function *k.p* formalism [7]. Such empirical approaches are successful while describing conduction band, yet fails for the valence band representing the heavy-hole. The failure of these methods is due to the fact that these approaches do not take into account the curvature and anisotropy of the remote bands. In this chapter, based on first-principle method, the electronic band structures and optical spectra of bulk In(As,Sb) and that of InAs/$InAs_{0.625}Sb_{0.375}$ SLs are explored with the lattice constants of bulk InAs, GaSb and AlSb, respectively. The results manifest higher absorption coefficients for SLs with respect to bulk counterpart, which reconfirms the dominance of the 3D SLs in detector applications. Further, the effective masses computed for heavy-holes in the k_x-k_y plane are reduced in the case of superlattice, which suggest that III-V SLs could possibly replace IV-VI materials as efficient Pb-free infrared detectors. The InAs and InSb are the III-V zinc-blende compounds with semiconducting behavior. For these compounds and alloys, the growth of heterostructures and superlattices is possible, wherein through alloy composition, thickness, and the interface chemistry one can modulate the electronic band gaps and their bandwidths [136]. There exists type-II band alignment in InAs/In(As,Sb) SLs, where the electrons are found in InAs part, while the holes are confined in the In(As,Sb) layers, indicating that electrons and holes are separated spatially. Consequently, with the adjustment of InAs thickness or that of In(As,Sb) or the concentration of Sb, the band gap can be tuned for a broad range of infrared detecting region. Due to these characteristics, we have chosen the T2SLs of InAs/In(As,Sb) for far-infrared applications. To this end, we first perform the DFT calculations using spin-orbit coupling and modified Becke-Johnson (MBJ), for the bulk In(As,Sb) and then consider a large 3D superlattice. On top of this, the optical properties are calculated, making our approach quite demanding from computational perspective.

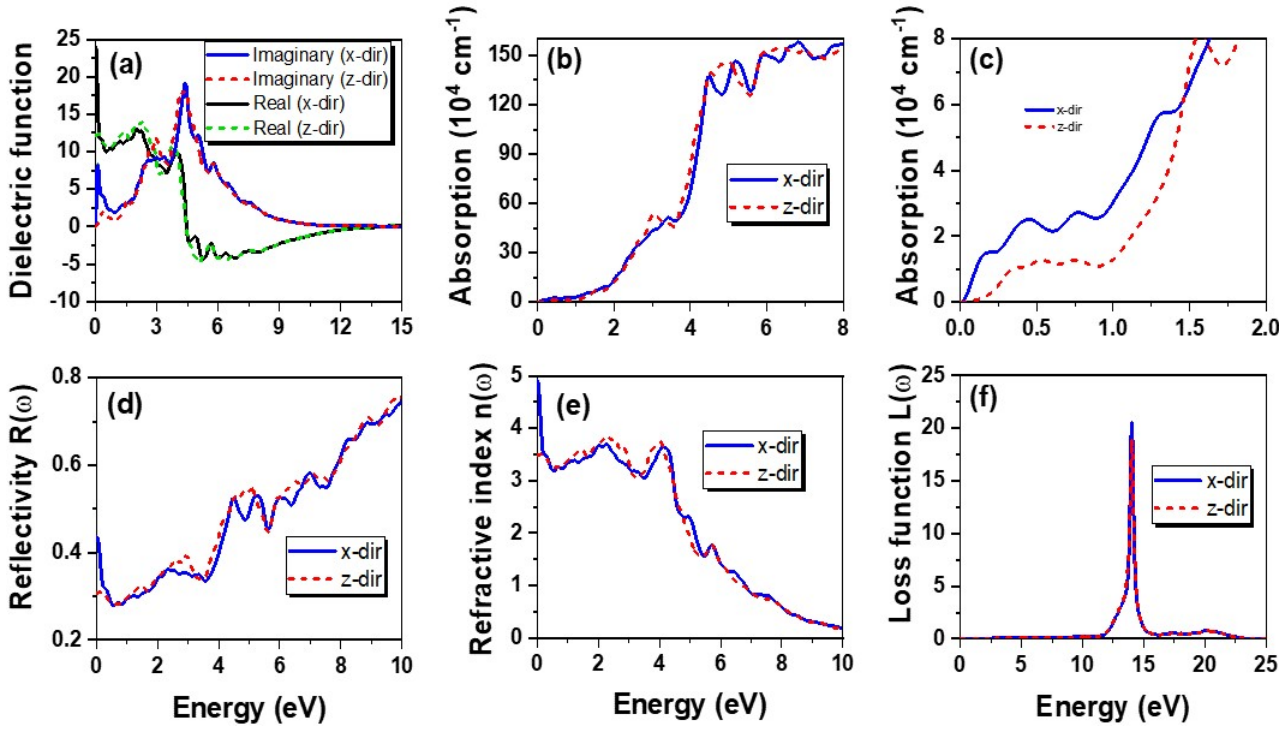

FIG. 3. Frequency-dependent optical properties of InAs/$InAs_{0.625}Sb_{0.375}$ superlattice with lattice constant at T=300 K that is a_{GaSb}=6.0959 Å. (a) Real and imaginary parts of the dielectric function. (b) Absorption spectra in the frequency-range between 0 and 8 eV. (c) Absorption spectra in the IR region. (d) Reflectivity. (e) Refractive index. (f) Energy loss function. The x-dir and z-dir indicate the directions of the electric field polarized perpendicular and parallel to c-axis of the SL.

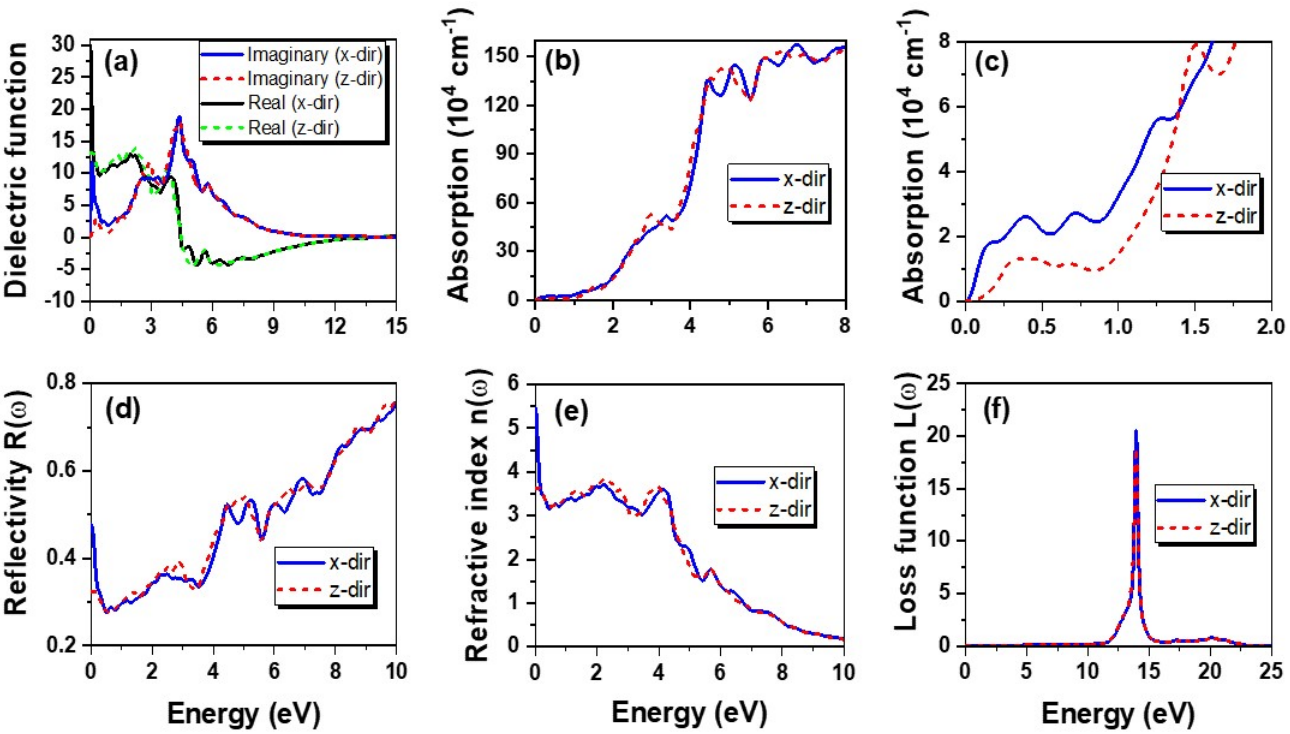

FIG. 4. Frequency-dependent optical properties of InAs/$InAs_{0.625}Sb_{0.375}$ superlattice with lattice constant at T=300 K that is a_{AlSb}=6.1355 Å. Real and imaginary parts of the dielectric function. (b) Absorption spectra in the frequency-range between 0 and 8 eV. (c) Absorption spectra in the IR region. (d) Reflectivity. (e) Refractive index. (f) Energy loss function. The x-dir and z-dir indicate the directions of the electric field polarized perpendicular and parallel to c-axis of the SL.

3.3 PAPER II: 2D materials and heterostructures

The exceptional crystal structures of 2D TMDs and their outstanding electronic attributes make them potential materials in applications including electronics, photonics, and optoelectronics [79-82]. Intriguingly, upon integration of 2D materials with other 2D structures in the form of heterostructures are exemplified to be quite appealing. Specifically, the 2D TMDs could be skillfully bring-together thereby fabricating various heterostructures or superlattices possessing exotic properties that cannot be acquired from isolated 2D material, thus providing the opportunities to explore and investigate the novel applications for the nanodevices [83-85]. The hybrid structures between the different 2D materials can be obtained using different approaches, for instance, the mechanical exfoliation followed by the pick-up-and-transfer technique can be used to create 2D layered heterostructures, but chemical vapor deposition (CVD) enables the direct growth of TMDs layers that are lattice aligned for the heterostructures. Moreover, the monolayer TMD on a wide scale can be synthesized on large scale with seeding promoter-assisted-CVD. Based on the choice of seeding promoter and its capacity to adhere to substrates, this strategy was subsequently adapted for the construction of a range of vertical and lateral hybrid-structures. Besides, it is demonstrated that the technique is independent of lattice mismatch among the combining materials (2D and TMD) to create vertical or lateral heterostructures [91-93, 137]. One-step or two-step CVD synthesis have both been used to effectively produce a number of lateral heterostructures, including MoS_2/WSe_2, NbS_2/MoS_2, $MoS_2/MoSe_2$, and $ReS_2/ReSe_2$, MoS_2/WS_2.

A novel class of 2D materials MA_2Z_4, (where M represents a Transition metal, A stands for group IV element, while Z is group V element) has received considerable attention owing to their exceptional properties [117]. The $MoSi_2N_4$ is first 2D material of this group, which was successfully grown using the CVD method over a big surface of 15 mm by 15 mm. This septuple-atomic-layer semiconducting material (N-Si-N-Mo-N-Si-N) may be viewed of as the three atom thick MoN_2 sandwiched between the two SiN layers with indirect band gap of about 1.94 eV. The elastic modulus of a monolayer of $MoSi_2N_4$ is about four times greater than that of a single layer of MoS_2, and the carrier mobilities of holes and electrons are correspondingly four to six times greater. Moreover, calculations using density functional theory predict the existence of a novel family called MA_2Z_4 (M is Transition metal, A is IV element, and Z is V element). The extraordinary attributes of these materials have been the subject of several research to date [118, 119, 121, 122, 124, 125, 138, 139]. Motivated by the previously reported 2D materials and their heterostructures, we investigate here the 2D monolayers XSi_2N_4 (X = Mo, W, and Ti), and the vertical and lateral heterostructures ($MoSi_2N_4/WSi_2N_4$, and $MoSi_2N_4/TiSi_2N_4$) of this new family. Both, the monolayers and heterostructures are thermodynamically stable with outstanding electronic properties. From the electronic band structures, we noticed that the band gap varies from the visible to infrared region employing their applications in different optoelectronic devices.

3.4 PAPER III: Strain modulated electro-optical properties of laterally stitched 2D heterostructures

This article is the extension of paper II exclusively focusing on the laterally stitched 2D heterostructures $MoSi_2N_4/XSi_2N_4$ (X=W, Ti). These systems being energetically and dynamically stable with unique electronic features further motivated us to study the tuning of electronic and optical properties. Such heterostructures due to their unique quality of interfaces and their distinctive electrostatics have recently attracted a lot of research interest [94]. The parallel stitched heterostructures of 2D materials are superior to vertical and bulk hetero-systems in that they have larger depletion region, and therefore are more sensitive to charge fluctuation [98, 99], making them perfect for optoelectronic applications [100, 101].

While the $MoSi_2N_4/TiSi_2N_4$ lateral heterostructure (MTLH) exhibits a bandgap of 0.343 eV, the $MoSi_2N_4/WSi_2N_4$-lateral heterostructure (MWLH) reveals a bandgap of 2.35 eV. Further, the impact of biaxial strain on the electronic and optical characteristics of MWLH and MTLH revealed significant changes in their spectra. For instance, the compressive strain in MTLH results in a change from semiconducting to metallic, whereas that in MWLH results in an indirect to direct bandgap transition. Biaxial strain may also be used to successfully modify the spectra of absorbance, transmittance, and reflection. Our research sheds light on the strain engineering of electro-optical properties, opening the door for potential nano- and optoelectronic applications in the future.

Supplementary materials

Strain modulated electronic and optical properties of laterally stitched $MoSi_2N_4/XSi_2N_4$ (X=W, Ti) 2D heterostructures

Ghulam Hussain,[a,*] Mumtaz Manzoor,[b] Muhammad Waqas Iqbal,[b] Imran Muhammad,[c] Asadollah Bafekry,[d,*] Hamid Ullah,[b,*] Carmine Autieri[a]

[a]International Research Centre MagTop, Institute of Physics, Polish Academy of Sciences, Aleja Lotników 32/46, PL-02668 Warsaw, Poland

[b]Department of Physics, Riphah International University, Campus Lahore, Pakistan

[c]School of Materials Science and Engineering, CAPT, Peking University, Beijing 100871, China

[d]Department of Physics, University of Antwerp, Groenenborgerlaan 171, B-2020 Antwerp, Belgium

E-mail: ghussain@ifpan.edu.pl, bafekry.asad@gmail.com, hamid.ullah@riphah.edu.pk

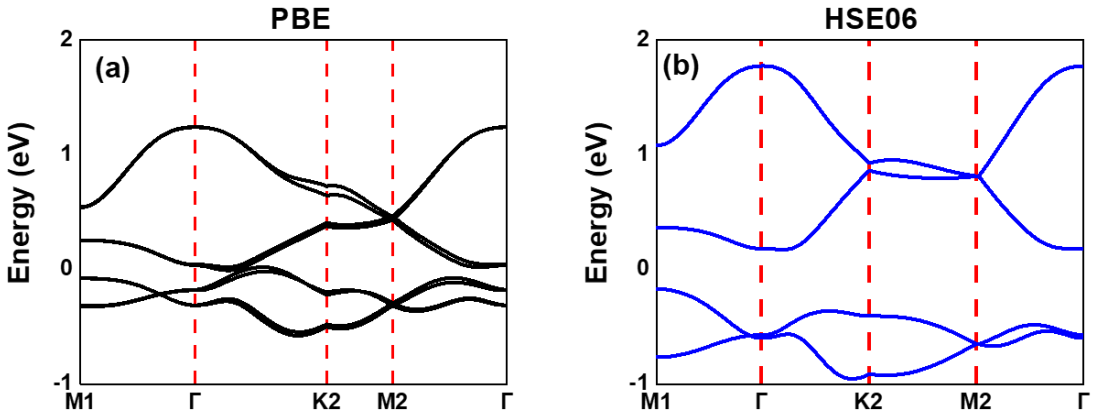

Figure S1 (a) Bandstructure of MTLH along the k-path (M1-Γ-K2-M2-Γ), the VBM and CBM cross the Fermi-level, indicating the metallic behavior. (b) HSE06 based bandstructure for MTLH.

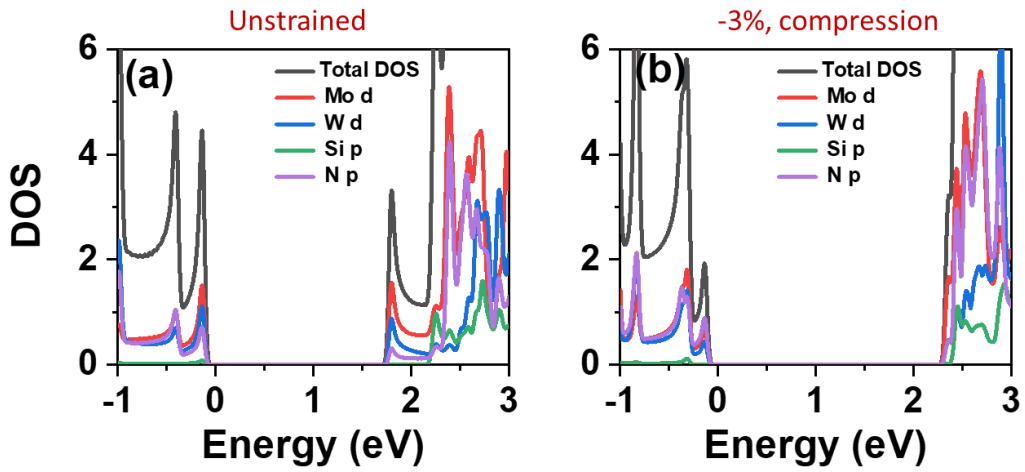

Figure S2 Partial density of states (PDOS), (a) Unstrained MWLH, (b) -3% strained MWLH.

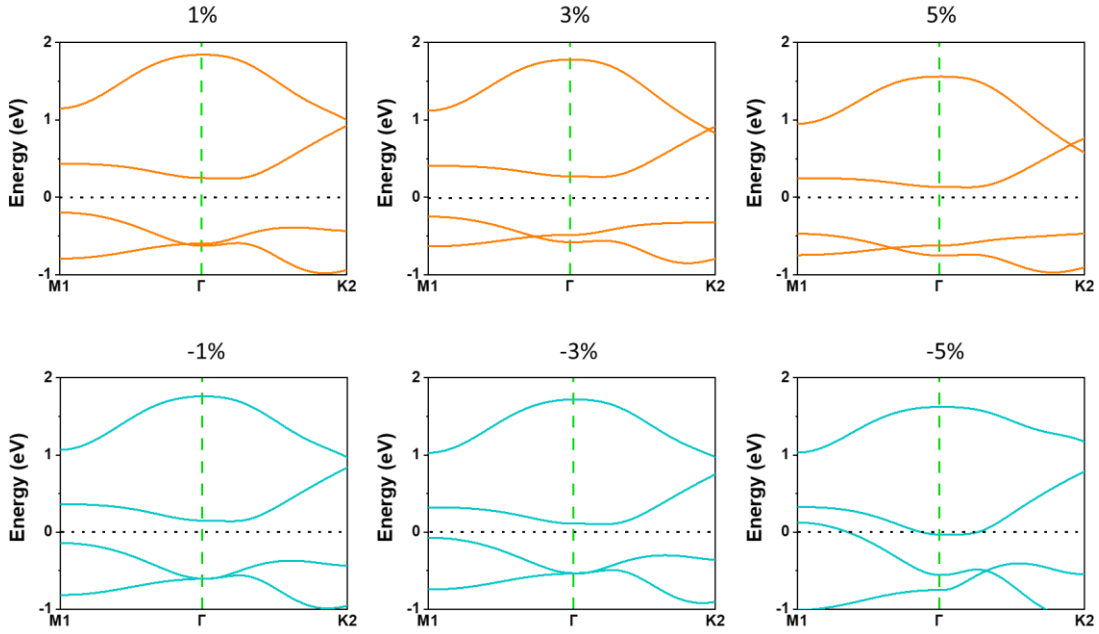

Figure S3 Strain modulated electronic band structures of MTLHs using HSE06. The magnitude of applied strain is indicated for each figure in percent. The black dashed line indicate the position of Fermi level (which is set to zero).

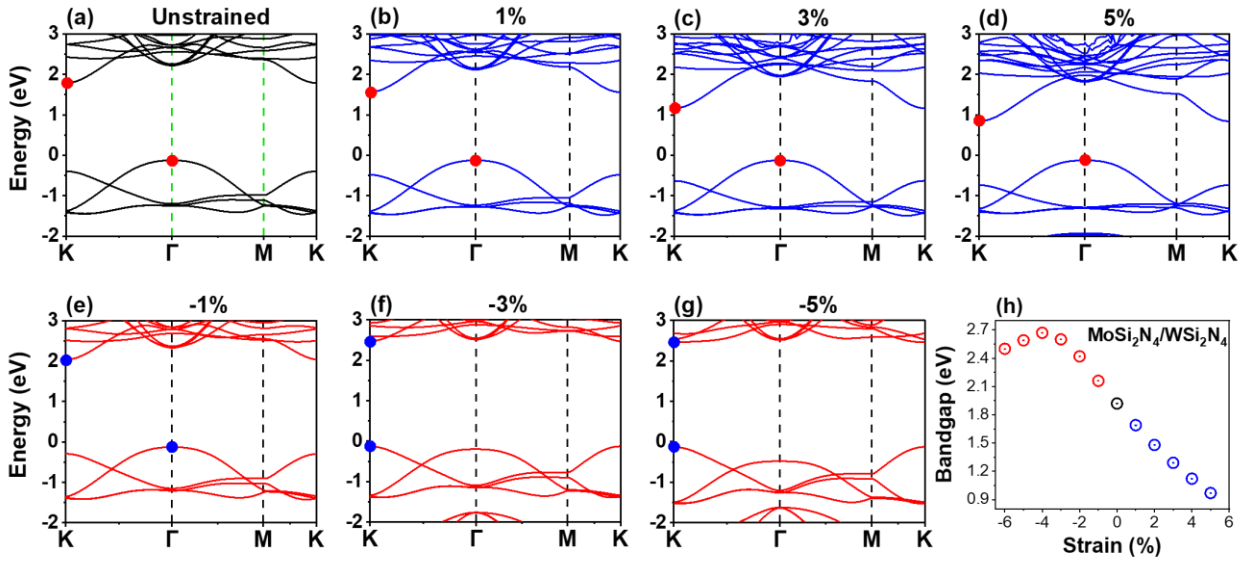

Figure S4 Electronic band structures of MWLHs without SOC. The black in (a) demonstrates the bandstructure of unstrained MWLH, while the blue curves in (b), (c) and (d) show the bandstructures for successive tensile biaxial strains. Figures (e)-(g) represent the bandstructures of MWLH against compression. (h) The trend of electronic bandgap versus biaxial strain.

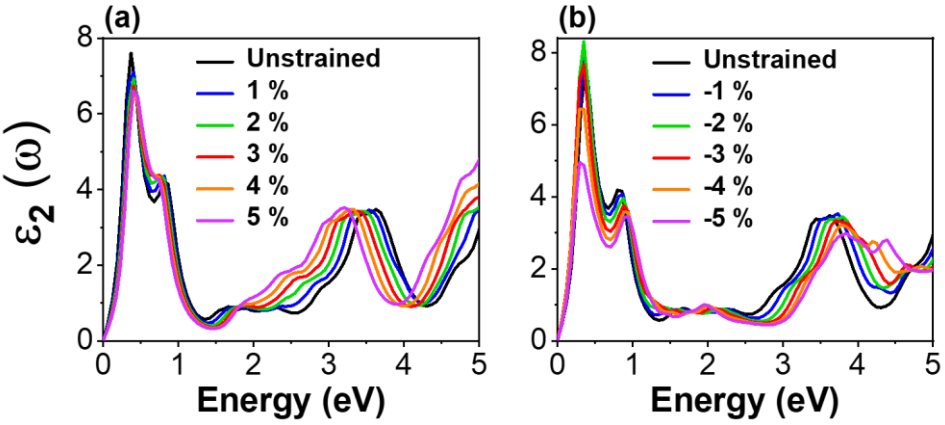

Figure S5 Imaginary part of dielectric function for MTLH as a function of biaxial strain, the peaks in the spectrum correspond to the possible interband transitions from valence to conduction bands.

3.5 PAPER IV: Janus structures

2D transition metal chalcogenides structures have undergone substantial research and found a wide range of uses in electronics and optoelectronics [70, 102-104, 140-144]. The transition metal dichalcogenides (TMDs) bearing the bandgaps ranging from 1.1–1.9 eV with promising mechanical and electronic properties make them suitable to use these systems in photonics and electronic devices [69, 73, 76, 80, 105, 106, 145, 146]. At the corners of the hexagonal Brillouin zone of TMDs, there exist high spin splitting due to the absence of inversion symmetry, and significant spin-orbit coupling (SOC), which is produced by the d-orbitals of transition metals in TMDs [73-75]. Because of the strong correlation between the spin and valley degrees of freedom, the TMDs are regarded as the optimal materials in valleytronics [76, 78, 147]. Additionally, the alloy composition in TMDs, such as in $Mo_xW_{1-x}S_2$, $WS_{2x}Se_{2-2x}$ and MoS_xSe_{2-x}, might be used to modify the electrical and optical characteristics [107-111]. Recently, the chemical vapor deposition (CVD) approach has been used to successfully develop the Janus phase of MoSSe in the 2H phase [112, 113], where the S layer is replaced with Se atoms in the case of MoS_2, while the Se layer with S atoms in $MoSe_2$. With respect to MX_2 (M=Mo, W, and X=S, Se) that preserves the mirror symmetry, the Janus structure i.e. MXY (M=W, Mo, X=Se, S, and Y=S, Se) breaks this symmetry displaying an out-of-plane piezoelectricity and Rashba-type spin splitting due to the perpendicular electric field that results from the breaking of mirror symmetry [72, 114-116, 148].

In this paper, encouraged from the excellent features of MA_2Z_4 materials introduced in paper II and III, we investigate here other members of this family such as pristine $MoSi_2P_4$ and Janus $XGeSiP_2As_2$ (X = Mo, W) monolayers. Using the relativistic density functional theory, the phonon band structures and the orbital-projected electronic band structures are computed thereby to study the dynamical stability and electronic properties. We observed the Zeeman type spin-splitting at K/K' and Rashba-type spin split states at the Γ-point of the Brillouin zone in Janus monolayers. Further exploring these features, we determined the in-plane and out-of-plane spin textures. Due to the breaking of mirror symmetry, we noticed reduced direct bandgaps and large spin-split states in the Janus $XGeSiP_2As_2$ (X = Mo, W) structures along with Rashba splitting, as compared to pristine $MoSi_2P_4$. In the supplementary material, we show and compare the optical spectra for pristine and Janus phases and explain how these materials could be useful in the infrared detectors. The unique electronic, spin and Rashba-type features together with the exceptional optical spectra offer the possibility to employ these systems in the valleytronics, spintronics and optoelectronics.

Emergence of Rashba splitting and spin-valley properties in Janus $MoGeSiP_2As_2$ and $WGeSiP_2As_2$ monolayers

Ghulam Hussain,[a,*] Abdus Samad,[b] Majeed Ur Rehman,[c,*] Giuseppe Cuono,[a] Carmine Autieri[a]

[a]International Research Centre MagTop, Institute of Physics, Polish Academy of Sciences, Aleja Lotnikow 32/46, PL-02668 Warsaw, Poland

[b]Department of Physics and Energy Harvest Storage Center, University of Ulsan, Ulsan 44610, South Korea

[c]College of Physics and Optoelectronic Engineering, Shenzhen University, Shenzhen, Guangdong 518060, China

E-mail: ghussain@ifpan.edu.pl, majeed@mail.ustc.edu.cn

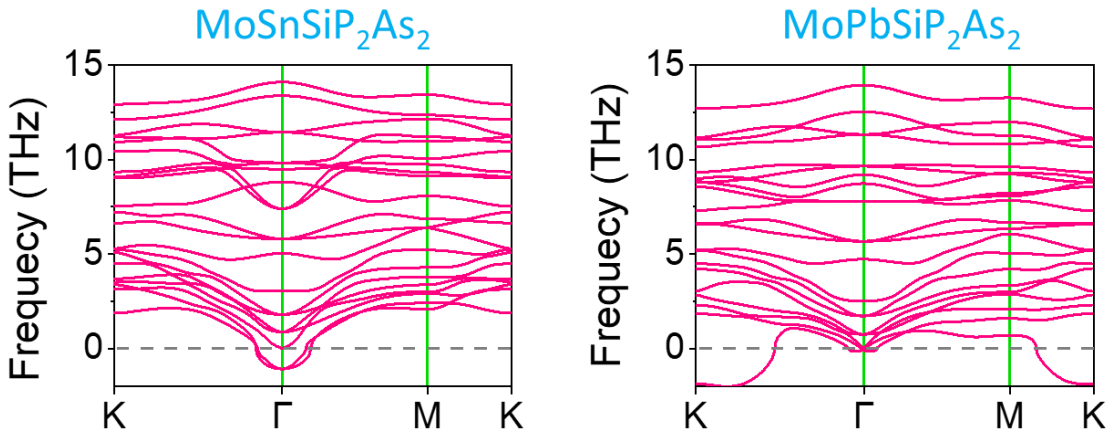

Figure S1 Phonon spectra of Janus $MoSnSiP_2As_2$ and $MoPbSiP_2As_2$ monolayers. Since, the structures show negative phonon modes, they are dynamically unstable.

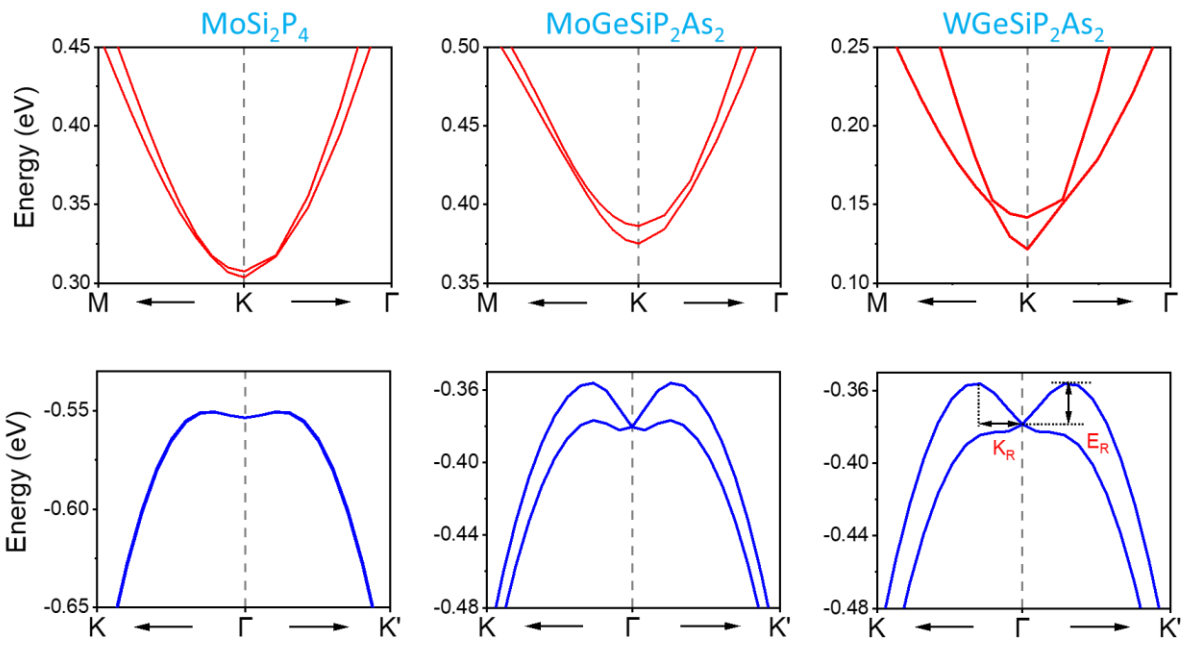

Figure S2 Zoomed illustrations of the conduction band split states λ_{Kc} at K-point, and that of valence band at Γ-point for the pristine and Janus phases to investigate the Rashba-type spin splitting.

Optical spectra

In studying the optical properties, the dielectric function of a material is a unique feature that describes the interaction of an oscillating light wave in the form of electric field with the material. The dielectric function can be used to derive other linear optical features, for instance, in Fig. S3, the plots for the absorbance and reflectance are illustrated. Using PBE functional, we computed the absorbance spectra of monolayer $MoSi_2P_4$ in pristine and Janus $XGeSiP_2As_2$ structures as shown. We noticed that both the pristine as well as Janus phases have characteristic absorption peaks in the infra-red region, which correspond to direct optical transitions in the band structures (e.g. the first absorbance peaks occur at the photon energies equal to the electronic band gaps at the K-point). Intriguingly, the first absorbance peak is red-shifted to 0.25 eV ($WGeSiP_2As_2$) from 0.57 eV ($MoGeSiP_2As_2$) offering the possibility to tune the IR range. In addition, for pristine

$MoSi_2P_4$ this corresponds to a wavelength of 2 μm, while for the Janus phase of $WGeSiP_2As_2$ this corresponds to a wavelength of ~5 μm employing their applications in the near- and mid-IR detector applications, respectively. Moreover, we show the reflectance spectra for the pristine and Janus structures in Fig S3(b), which indicate almost negligible reflectance in the IR range, and thus employ their utilization in the IR photo-detector devices.

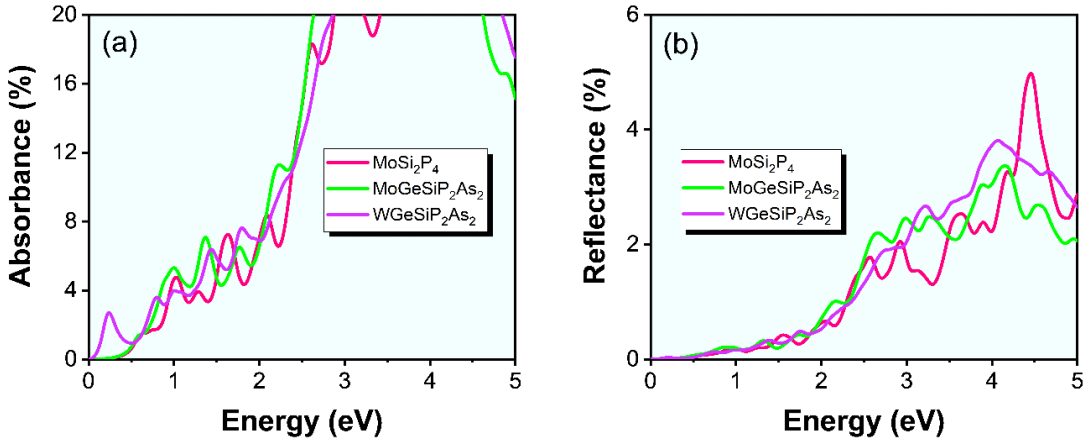

Figure S3 Comparison of the optical spectra of pristine $MoSi_2P_4$ with those of Janus $XGeSiP_2As_2$ structures indicated (a) Absorbance, and (b) Reflectance.

Chapter 6

CONCLUSIONS

In summary, using the first-principles calculations, we have investigated the optoelectronic features of 3D InAs/$InAs_{0.625}Sb_{0.375}$ SLs, 2D materials XSi_2N_4 (Mo, W, Ti) and their heterostructures, and Janus structures, respectively. We propose these materials as feasible optoelectronic materials that covers the range from far-IR to visible part of electromagnetic spectrum. While studying the electronic and optical attributes, we noticed significant variations as we moved from bulk InAs, InSb to the InAs/$InAs_{0.625}Sb_{0.375}$ SLs. Also, the properties are strongly depending on the lattice constant of the superlattice, which can be tuned effectively to cover the different regions of far-detection. The existence of two heavy-hole bands with increasing in-plane effective mass as one goes far from the Fermi level is observed. Besides, we noted a substantial decrease in the effective masses of heavy-holes, and energy gaps in the k_x-k_y plane with respect to their bulk counterpart. We discovered that the electrons are delocalized in the InAs part of SL, while the holes are localized in the $InAs_{0.625}Sb_{0.375}$ part giving rise to type II superlattice. Moreover, the absorption spectra in the far-infrared regime are strongly increased for InAs/$InAs_{0.625}Sb_{0.375}$ SLs as compared to bulk InAs and InSb suggesting their suitability in IR photodetectors.

Together with the 3D superlattice, we successfully demonstrated the thermodynamical stability of the novel 2D materials family, their heterostructures and Janus structures. We performed computationally demanding calculations for the realistic systems combining spin-orbit coupling, HSE functional and the strain induced engineering of electro-optical properties. It is established that the monolayers and the heterostructures are stable and experimentally accessible as confirmed by the total energy ground state calculations and the phonon spectra. After confirming the structural stability, we presented the electronic band structures and the density of states for the monolayered materials such as XSi_2N_4 (M = Mo, W, and Ti), and their 2D heterostructures $MoSi_2N_4/XSi_2N_4$, (X=W, Ti) revealing a semiconducting behavior with the band gaps ranging from the infrared to the visible region. The band structure for $MoSi_2N_4/WSi_2N_4$ heterostructure exposed that its bandgap lies in the visible region employing their applications for photovoltaics and other optoelectronic devices. However, for 'Ti' incorporated heterostructure ($MoSi_2N_4/TiSi_2N_4$) the band gap drops to the IR range providing the opportunity to utilize these heterostructures as IR detector materials. In addition, the effect of biaxial strain on the

optoelectronic properties of laterally stitched 2D heterostructures manifested significant modifications in the electronic band structures and optical properties. We noticed that the compressive strain causes a transition from indirect to direct band gap semiconductor in $MoSi_2N_4/WSi_2N_4$, while a semiconducting to metallic transition in $MoSi_2N_4/TiSi_2N_4$. Besides, the optical spectra including absorbance, transmittance and reflectance can be tuned efficiently using biaxial strain. Our findings based on the electro-optical properties and their controlled modulation via biaxial strain suggest the applications of these newly discovered 2D materials and heterostructures in nano- and optoelectronics.

Lastly, an explicit study on the pristine $MoSi_2P_4$ and Janus $XGeSiP_2As_2$ (X = Mo, W) monolayers of these recently discovered 2D materials is carried out. Both, the pristine and Janus phases were demonstrated to be thermodynamically. We observed an intrinsic spin splitting at the K/K'-points of the pristine $MoSi_2P_4$ in the electronic band structures, which is further enhanced in the Janus structure, suggesting their valleytronic applications. In addition, the broken mirror symmetry in Janus phase induces an out-of-plane electric field that results in splitting of valence bands at the Γ-point not only in energy but also in momentum space, a signature of Rashba-type spin splitting, which occurs due to the asymmetric potential in the Janus phase, perpendicular to the basal plane. Moreover, we noticed characteristic absorption peaks in the infra-red region for both the pristine as well as the Janus phases (shown in supplementary material) employing their use in the IR devices. The large spin and Rashba-type splittings together with the exceptional optical spectra in these structures can make extraordinary contribution in the valleytronics, spintronics and IR applications.

References

1. Adams, F. and C. Barbante, *Nanotechnology and analytical chemistry*, in *Comprehensive Analytical Chemistry*. 2015, Elsevier. p. 125-157.
2. Herschel, W., *XIV. Experiments on the refrangibility of the invisible rays of the sun.* Philosophical Transactions of the Royal Society of London, 1800(90): p. 284-292.
3. Barr, E.S., *Historical survey of the early development of the infrared spectral region.* American Journal of physics, 1960. **28**(1): p. 42-54.
4. Barr, E.S., *The infrared pioneers—I. Sir William Herschel.* Infrared Physics, 1961. **1**: p. 1-2.
5. Barr, E.S., *The infrared pioneers—II. Macedonio melloni.* Infrared physics, 1962. **2**(2): p. 67-74.
6. Hudson, R.D., *Infrared system engineering*. Vol. 1. 1969: Wiley-Interscience New York.
7. Rogalski, A., *History of infrared detectors.* Opto-Electronics Review, 2012. **20**(3): p. 279-308.
8. Barr, E.S., *The infrared pioneers—III. Samuel pierpont Langley.* Infrared physics, 1963. **3**(4): p. 195-206.
9. Langley, S.P. *The bolometer and radiant energy*. in *Proceedings of the American Academy of Arts and Sciences*. 1880. JSTOR.
10. Walcott, C.D., *Biographical Memoir of Samuel Pierpont Langley, 1834-1906*. Vol. 7. 1912: National Academy of Sciences.
11. Hertz, H., *Ueber einen Einfluss des ultravioletten Lichtes auf die electrische Entladung.* Annalen der Physik, 1887. **267**(8): p. 983-1000.
12. Elster, J. and H. Geitel, *Ueber die Entladung negativ electrischer Körper durch das Sonnen-und Tageslicht.* Annalen der Physik, 1889. **274**(12): p. 497-514.
13. Case, T.W., *Notes on the change of resistance of certain substances in light.* Physical Review, 1917. **9**(4): p. 305.
14. Kruse, P.W., L.D. McGlauchlin, and R.B. McQuistan, *Elements of infrared technology: Generation, transmission and detection.* New York: Wiley, 1962.
15. Cashman, R., *Film-type infrared photoconductors.* Proceedings of the IRE, 1959. **47**(9): p. 1471-1475.
16. Lovell, D., *Cashman thallous sulfide cell.* Applied optics, 1971. **10**(5): p. 1003-1008.
17. Lovell, D., *The development of lead salt detectors.* American Journal of Physics, 1969. **37**(5): p. 467-478.
18. Rollin, B. and E. Simmons, *Long Wavelength Infra-Red Photoconductivity of Silicon at Low Temperatures.* Proceedings of the Physical Society. Section B, 1952. **65**(12): p. 995.

19. Burstein, E., J. Oberly, and J. Davisson, *Infrared photoconductivity due to neutral impurities in silicon.* Physical Review, 1953. **89**(1): p. 331.
20. Borrello, S.R. and H. Levinstein, *Preparation and Properties of Mercury-Doped Germanium.* Journal of Applied Physics, 1962. **33**(10): p. 2947-2950.
21. Biberman, L. and R. Sendall, *Introduction: A brief history of imaging devices for night vision.* Electro-optical imaging: system performance and modelling, 2000.
22. Lawson, W., et al., *Preparation and properties of HgTe and mixed crystals of HgTe-CdTe.* Journal of Physics and Chemistry of Solids, 1959. **9**(3-4): p. 325-329.
23. Melngailis, I. and T. Harman, *Single-crystal lead-tin chalcogenides,* in *Semiconductors and Semimetals*. 1970, Elsevier. p. 111-174.
24. Harman, T. and I. Melngailis, *Narrow gap semiconductors,* in *Applied Solid State Science*. 1974, Elsevier. p. 1-94.
25. Dornhaus, R. and G. Nimtz, *The properties and applications of the Hg 1− x Cd x Te alloy system.* Narrow-Gap Semiconductors, 1983: p. 119-281.
26. Preier, H., *New aspects of the material and device technology of intrinsic infrared photodetectors,* in *Physics of Narrow Gap Semiconductors*. 1982, Springer. p. 280-282.
27. Long, D. and J.L. Schmit, *Mercury-cadmium telluride and closely related alloys,* in *Semiconductors and semimetals*. 1970, Elsevier. p. 175-255.
28. Smith, D. and C. Mailhiot, *Proposal for strained type II superlattice infrared detectors.* Journal of Applied Physics, 1987. **62**(6): p. 2545-2548.
29. Levine, B., *Quantum-well infrared photodetectors.* Journal of applied physics, 1993. **74**(8): p. R1-R81.
30. Rogalski, A., *Infrared detectors: status and trends.* Progress in quantum electronics, 2003. **27**(2-3): p. 59-210.
31. Schneider, H. and H.C. Liu, *Quantum well infrared photodetectors.* 2007.
32. Rogalski, A. and R. Ciupa, *Performance limitation of short wavelength infrared InGaAs and HgCdTe photodiodes.* Journal of electronic materials, 1999. **28**(6): p. 630-636.
33. Tidrow, M.Z., et al. *Device physics and focal plane array applications of QWIP and MCT.* in *Photodetectors: Materials and Devices IV*. 1999. SPIE.
34. Rogalski, A., P. Martyniuk, and M. Kopytko, *InAs/GaSb type-II superlattice infrared detectors: Future prospect.* Applied physics reviews, 2017. **4**(3): p. 031304.
35. Rogalski, A., et al., *InAsSb-based infrared photodetectors: Thirty years later on.* Sensors, 2020. **20**(24): p. 7047.
36. Ting, D.Z., et al., *InAs/InAsSb type-II strained-layer superlattice infrared photodetectors.* Micromachines, 2020. **11**(11): p. 958.
37. Ting, D.Z., et al., *Long wavelength InAs/InAsSb infrared superlattice challenges: A theoretical investigation.* Journal of Electronic Materials, 2020. **49**(11): p. 6936-6945.
38. Martyniuk, P., et al., *Theoretical modeling of XBn T2SLs InAs/InAsSb/B-AlSb longwave infrared detector operating under thermoelectrical cooling.* Optical and Quantum Electronics, 2020. **52**(2): p. 1-10.

39. Ting, D.Z., et al., *Advances in III-V semiconductor infrared absorbers and detectors.* Infrared Physics & Technology, 2019. **97**: p. 210-216.
40. Long, M., et al., *Palladium diselenide long-wavelength infrared photodetector with high sensitivity and stability.* ACS nano, 2019. **13**(2): p. 2511-2519.
41. Steenbergen, E., et al., *Significantly improved minority carrier lifetime observed in a long-wavelength infrared III-V type-II superlattice comprised of InAs/InAsSb.* Applied Physics Letters, 2011. **99**(25): p. 251110.
42. Klipstein, P., et al., *Modeling InAs/GaSb and InAs/InAsSb superlattice infrared detectors.* Journal of electronic materials, 2014. **43**(8): p. 2984-2990.
43. Lu, Q., W. Liu, and X. Wang, *2-D material-based photodetectors on flexible substrates.* Inorganic Flexible Optoelectronics: Materials and Applications, 2019: p. 117-142.
44. Moore, M., *International roadmap for devices and systems.* Accessed: Jan, 2020.
45. Bonaccorso, F., et al., *Graphene photonics and optoelectronics.* Nature photonics, 2010. **4**(9): p. 611-622.
46. Li, X., et al., *Graphene and related two-dimensional materials: Structure-property relationships for electronics and optoelectronics.* Applied Physics Reviews, 2017. **4**(2): p. 021306.
47. Bae, S., et al., *Roll-to-roll production of 30-inch graphene films for transparent electrodes.* Nature nanotechnology, 2010. **5**(8): p. 574-578.
48. Akinwande, D., N. Petrone, and J. Hone, *Two-dimensional flexible nanoelectronics.* Nature communications, 2014. **5**(1): p. 1-12.
49. Xia, F., et al., *Ultrafast graphene photodetector.* Nature nanotechnology, 2009. **4**(12): p. 839-843.
50. Wang, G., et al., *Two dimensional materials based photodetectors.* Infrared Physics & Technology, 2018. **88**: p. 149-173.
51. Grigorenko, A.N., M. Polini, and K. Novoselov, *Graphene plasmonics.* Nature photonics, 2012. **6**(11): p. 749-758.
52. Sun, Z., et al., *Graphene mode-locked ultrafast laser.* ACS nano, 2010. **4**(2): p. 803-810.
53. Liu, M., et al., *A graphene-based broadband optical modulator.* Nature, 2011. **474**(7349): p. 64-67.
54. Rogalski, A., M. Kopytko, and P. Martyniuk, *Two-dimensional infrared and terahertz detectors: Outlook and status.* Applied Physics Reviews, 2019. **6**(2): p. 021316.
55. Nicolosi, V., et al., *Liquid exfoliation of layered materials.* Science, 2013. **340**(6139): p. 1226419.
56. Zhang, B., et al., *Recent progress in 2D material-based saturable absorbers for all solid-state pulsed bulk lasers.* Laser & Photonics Reviews, 2020. **14**(2): p. 1900240.
57. Wang, J., et al., *Recent progress on localized field enhanced two-dimensional material photodetectors from ultraviolet—visible to infrared.* Small, 2017. **13**(35): p. 1700894.
58. Buscema, M., et al., *Photocurrent generation with two-dimensional van der Waals semiconductors.* Chemical Society Reviews, 2015. **44**(11): p. 3691-3718.

59. Long, M., et al., *Progress, challenges, and opportunities for 2D material based photodetectors.* Advanced Functional Materials, 2019. **29**(19): p. 1803807.
60. Wang, F., et al., *2D library beyond graphene and transition metal dichalcogenides: a focus on photodetection.* Chemical Society Reviews, 2018. **47**(16): p. 6296-6341.
61. Cheng, J., et al., *Recent advances in optoelectronic devices based on 2D materials and their heterostructures.* Advanced Optical Materials, 2019. **7**(1): p. 1800441.
62. Britnell, L., et al., *Strong light-matter interactions in heterostructures of atomically thin films.* Science, 2013. **340**(6138): p. 1311-1314.
63. Dai, Z., L. Liu, and Z. Zhang, *Strain engineering of 2D materials: issues and opportunities at the interface.* Advanced Materials, 2019. **31**(45): p. 1805417.
64. Pi, L., et al., *Recent progress on 2D noble-transition-metal dichalcogenides.* Advanced Functional Materials, 2019. **29**(51): p. 1904932.
65. Zhang, W., et al., *Two-dimensional semiconductors with possible high room temperature mobility.* Nano Research, 2014. **7**(12): p. 1731-1737.
66. Zhao, Y., et al., *High-electron-mobility and air-stable 2D layered PtSe2 FETs.* Advanced Materials, 2017. **29**(5): p. 1604230.
67. Kuc, A., N. Zibouche, and T. Heine, *Influence of quantum confinement on the electronic structure of the transition metal sulfide T S 2.* Physical Review B, 2011. **83**(24): p. 245213.
68. Kumar, A. and P. Ahluwalia, *Electronic structure of transition metal dichalcogenides monolayers 1H-MX2 (M= Mo, W; X= S, Se, Te) from ab-initio theory: new direct band gap semiconductors.* The European Physical Journal B, 2012. **85**(6): p. 1-7.
69. Mak, K.F. and J. Shan, *Photonics and optoelectronics of 2D semiconductor transition metal dichalcogenides.* Nature Photonics, 2016. **10**(4): p. 216-226.
70. Radisavljevic, B., et al., *Single-layer MoS2 transistors.* Nature nanotechnology, 2011. **6**(3): p. 147-150.
71. Eda, G. and S.A. Maier, *Two-dimensional crystals: managing light for optoelectronics.* ACS nano, 2013. **7**(7): p. 5660-5665.
72. Cheng, Y., et al., *Spin-orbit–induced spin splittings in polar transition metal dichalcogenide monolayers.* EPL (Europhysics Letters), 2013. **102**(5): p. 57001.
73. Kuc, A. and T. Heine, *The electronic structure calculations of two-dimensional transition-metal dichalcogenides in the presence of external electric and magnetic fields.* Chemical Society Reviews, 2015. **44**(9): p. 2603-2614.
74. Zhu, Z.Y., Y.C. Cheng, and U. Schwingenschlögl, *Giant spin-orbit-induced spin splitting in two-dimensional transition-metal dichalcogenide semiconductors.* Physical Review B, 2011. **84**(15): p. 153402.
75. Zibouche, N., et al., *Transition-metal dichalcogenides for spintronic applications.* Annalen der Physik, 2014. **526**(9-10): p. 395-401.
76. Zeng, H., et al., *Valley polarization in MoS2 monolayers by optical pumping.* Nature nanotechnology, 2012. **7**(8): p. 490-493.

77. Mak, K.F., et al., *Control of valley polarization in monolayer MoS2 by optical helicity.* Nature nanotechnology, 2012. **7**(8): p. 494-498.
78. Xiao, D., et al., *Coupled spin and valley physics in monolayers of MoS 2 and other group-VI dichalcogenides.* Physical review letters, 2012. **108**(19): p. 196802.
79. Lv, R., et al., *Transition metal dichalcogenides and beyond: synthesis, properties, and applications of single-and few-layer nanosheets.* Accounts of chemical research, 2015. **48**(1): p. 56-64.
80. Wang, Q.H., et al., *Electronics and optoelectronics of two-dimensional transition metal dichalcogenides.* Nature nanotechnology, 2012. **7**(11): p. 699-712.
81. Novoselov, K., et al., *2D materials and van der Waals heterostructures.* Science, 2016. **353**(6298): p. aac9439.
82. Li, X., et al., *2D Re-Based Transition Metal Chalcogenides: Progress, Challenges, and Opportunities.* Advanced Science, 2020. **7**(23): p. 2002320.
83. Gong, C., et al., *Electronic and optoelectronic applications based on 2D novel anisotropic transition metal dichalcogenides.* Advanced Science, 2017. **4**(12): p. 1700231.
84. Withers, F., et al., *Light-emitting diodes by band-structure engineering in van der Waals heterostructures.* Nature materials, 2015. **14**(3): p. 301-306.
85. Liu, Y., et al., *Van der Waals heterostructures and devices.* Nature Reviews Materials, 2016. **1**(9): p. 1-17.
86. Liu, Z., et al., *In-plane heterostructures of graphene and hexagonal boron nitride with controlled domain sizes.* Nature nanotechnology, 2013. **8**(2): p. 119-124.
87. Roy, K., et al., *Graphene–MoS2 hybrid structures for multifunctional photoresponsive memory devices.* Nature nanotechnology, 2013. **8**(11): p. 826-830.
88. Yu, W.J., et al., *Highly efficient gate-tunable photocurrent generation in vertical heterostructures of layered materials.* Nature nanotechnology, 2013. **8**(12): p. 952-958.
89. Yu, W.J., et al., *Vertically stacked multi-heterostructures of layered materials for logic transistors and complementary inverters.* Nature materials, 2013. **12**(3): p. 246-252.
90. Li, M.-Y., et al., *Epitaxial growth of a monolayer WSe2-MoS2 lateral pn junction with an atomically sharp interface.* Science, 2015. **349**(6247): p. 524-528.
91. Chen, C., et al., *Synthesis of Large-Area Uniform MoS2–WS2 Lateral Heterojunction Nanosheets for Photodetectors.* ACS Applied Nano Materials, 2021. **4**(5): p. 5522-5530.
92. Swain, G., S. Sultana, and K. Parida, *A review on vertical and lateral heterostructures of semiconducting 2D-MoS 2 with other 2D materials: A feasible perspective for energy conversion.* Nanoscale, 2021. **13**(22): p. 9908-9944.
93. Ling, X., et al., *Parallel stitching of 2D materials.* Advanced materials, 2016. **28**(12): p. 2322-2329.
94. Li, M.-Y., et al., *Heterostructures based on two-dimensional layered materials and their potential applications.* Materials Today, 2016. **19**(6): p. 322-335.
95. Antonova, I., *Vertical heterostructures based on graphene and other 2D materials.* Semiconductors, 2016. **50**(1): p. 66-82.

96. Iannaccone, G., et al., *Quantum engineering of transistors based on 2D materials heterostructures.* Nature nanotechnology, 2018. **13**(3): p. 183-191.
97. Yu, J.H., et al., *Vertical heterostructure of two-dimensional MoS2 and WSe2 with vertically aligned layers.* Nano letters, 2015. **15**(2): p. 1031-1035.
98. Nipane, A., et al., *Electrostatics of lateral pn junctions in atomically thin materials.* Journal of Applied Physics, 2017. **122**(19): p. 194501.
99. Yu, H., A. Kutana, and B.I. Yakobson, *Carrier delocalization in two-dimensional coplanar p–n junctions of graphene and metal dichalcogenides.* Nano letters, 2016. **16**(8): p. 5032-5036.
100. Tian, H., et al., *Novel field-effect Schottky barrier transistors based on graphene-MoS2 heterojunctions.* Scientific reports, 2014. **4**(1): p. 1-9.
101. Miao, J., et al., *High-responsivity graphene/InAs nanowire heterojunction near-infrared photodetectors with distinct photocurrent on/off ratios.* small, 2015. **11**(8): p. 936-942.
102. Chhowalla, M., et al., *The chemistry of two-dimensional layered transition metal dichalcogenide nanosheets.* Nature chemistry, 2013. **5**(4): p. 263-275.
103. Manzeli, S., et al., *2D transition metal dichalcogenides.* Nature Reviews Materials, 2017. **2**(8): p. 1-15.
104. Lei, W., et al., *Structural transition, metallization, and superconductivity in quasi-two-dimensional layered Pd S 2 under compression.* Physical Review B, 2020. **101**(20): p. 205149.
105. Iqbal, M.W., et al., *High-mobility and air-stable single-layer WS2 field-effect transistors sandwiched between chemical vapor deposition-grown hexagonal BN films.* Scientific reports, 2015. **5**(1): p. 1-9.
106. Ye, Z., et al., *Probing excitonic dark states in single-layer tungsten disulphide.* Nature, 2014. **513**(7517): p. 214-218.
107. Xi, J., et al., *Tunable electronic properties of two-dimensional transition metal dichalcogenide alloys: a first-principles prediction.* The journal of physical chemistry letters, 2014. **5**(2): p. 285-291.
108. Duan, X., et al., *Synthesis of WS2 x Se2–2 x alloy nanosheets with composition-tunable electronic properties.* Nano letters, 2016. **16**(1): p. 264-269.
109. Komsa, H.-P. and A.V. Krasheninnikov, *Two-dimensional transition metal dichalcogenide alloys: stability and electronic properties.* The journal of physical chemistry letters, 2012. **3**(23): p. 3652-3656.
110. Gong, Y., et al., *Band gap engineering and layer-by-layer mapping of selenium-doped molybdenum disulfide.* Nano letters, 2014. **14**(2): p. 442-449.
111. Lin, Z., et al., *Facile synthesis of MoS2 and MoxW1-xS2 triangular monolayers.* Apl Materials, 2014. **2**(9): p. 092514.
112. Zhang, J., et al., *Janus monolayer transition-metal dichalcogenides.* ACS nano, 2017. **11**(8): p. 8192-8198.

113. Lu, A.-Y., et al., *Janus monolayers of transition metal dichalcogenides.* Nature nanotechnology, 2017. **12**(8): p. 744-749.
114. Yao, Q.-F., et al., *Manipulation of the large Rashba spin splitting in polar two-dimensional transition-metal dichalcogenides.* Physical review B, 2017. **95**(16): p. 165401.
115. Li, F., et al., *Electronic and optical properties of pristine and vertical and lateral heterostructures of Janus MoSSe and WSSe.* The journal of physical chemistry letters, 2017. **8**(23): p. 5959-5965.
116. Hu, T., et al., *Intrinsic and anisotropic Rashba spin splitting in Janus transition-metal dichalcogenide monolayers.* Physical Review B, 2018. **97**(23): p. 235404.
117. Hong, Y.-L., et al., *Chemical vapor deposition of layered two-dimensional MoSi2N4 materials.* Science, 2020. **369**(6504): p. 670-674.
118. Lv, X., et al., *Strain modulation of electronic and optical properties of monolayer MoSi2N4.* Physica E: Low-dimensional Systems and Nanostructures, 2022. **135**: p. 114964.
119. Wu, Q., et al., *Semiconductor-to-metal transition in bilayer MoSi2N4 and WSi2N4 with strain and electric field.* Applied Physics Letters, 2021. **118**(11): p. 113102.
120. Wu, M. and J. Li, *Sliding ferroelectricity in 2D van der Waals materials: Related physics and future opportunities.* Proceedings of the National Academy of Sciences, 2021. **118**(50): p. e2115703118.
121. Islam, R., et al., *Switchable large-gap quantum spin Hall state in two-dimensional MSi $ _2 $ Z $ _4 $ materials class.* arXiv preprint arXiv:2207.08407, 2022.
122. Bafekry, A., et al., *MoSi2N4 single-layer: a novel two-dimensional material with outstanding mechanical, thermal, electronic and optical properties.* Journal of Physics D: Applied Physics, 2021. **54**(15): p. 155303.
123. Bafekry, A., et al., *Tunable electronic and magnetic properties of MoSi2N4 monolayer via vacancy defects, atomic adsorption and atomic doping.* Applied Surface Science, 2021. **559**: p. 149862.
124. Pham, D., *Electronic properties of a two-dimensional van der Waals MoGe 2 N 4/MoSi 2 N 4 heterobilayer: Effect of the insertion of a graphene layer and interlayer coupling.* RSC advances, 2021. **11**(46): p. 28659-28666.
125. Islam, R., et al., *Tunable spin polarization and electronic structure of bottom-up synthesized MoSi 2 N 4 materials.* Physical Review B, 2021. **104**(20): p. L201112.
126. Perdew, J.P., K. Burke, and M. Ernzerhof, *Generalized gradient approximation made simple.* Physical review letters, 1996. **77**(18): p. 3865.
127. Perdew, J.P., et al., *Atoms, molecules, solids, and surfaces: Applications of the generalized gradient approximation for exchange and correlation.* Physical review B, 1992. **46**(11): p. 6671.
128. Gupta, A., T. Sakthivel, and S. Seal, *Recent development in 2D materials beyond graphene.* Progress in Materials Science, 2015. **73**: p. 44-126.

129. Novoselov, K.S., et al., *Electric field effect in atomically thin carbon films.* science, 2004. **306**(5696): p. 666-669.
130. Geim, A.K. and K.S. Novoselov, *The rise of graphene*, in *Nanoscience and technology: a collection of reviews from nature journals*. 2010, World Scientific. p. 11-19.
131. Wu, D., et al., *High quantum efficiency mid-wavelength infrared type-II InAs/InAs1− xSbx superlattice photodiodes grown by metal-organic chemical vapor deposition.* Applied Physics Letters, 2019. **114**(1): p. 011104.
132. Moehle, C.M., et al., *InSbAs two-dimensional electron gases as a platform for topological superconductivity.* Nano Letters, 2021. **21**(23): p. 9990-9996.
133. Pikulin, D. and T. Hyart, *Interplay of exciton condensation and the quantum spin Hall effect in InAs/GaSb bilayers.* Physical Review Letters, 2014. **112**(17): p. 176403.
134. Winkler, G.W., et al., *Topological phases in InAs 1− x Sb x: from novel topological semimetal to Majorana wire.* Physical Review Letters, 2016. **117**(7): p. 076403.
135. Nguyen, N.M., et al., *Unprotected edge modes in quantum spin Hall insulator candidate materials.* arXiv preprint arXiv:2209.06912, 2022.
136. Mikhailova, M., K. Moiseev, and Y.P. Yakovlev, *Interface-induced optical and transport phenomena in type II broken-gap single heterojunctions.* Semiconductor science and technology, 2004. **19**(10): p. R109.
137. Hussain, G., et al., *Strain modulated electronic and optical properties of laterally stitched MoSi2N4/XSi2N4 (X= W, Ti) 2D heterostructures.* Physica E: Low-dimensional Systems and Nanostructures, 2022. **144**: p. 115471.
138. Zhong, T., et al., *Sliding ferroelectricity in two-dimensional MoA 2 N 4 (A= Si or Ge) bilayers: high polarizations and Moiré potentials.* Journal of Materials Chemistry A, 2021. **9**(35): p. 19659-19663.
139. Zhong, H., et al., *Strain-induced semiconductor to metal transition in m A 2 z 4 bilayers (m= Ti, Cr, Mo; a= Si; z= N, P).* Physical Review B, 2021. **103**(8): p. 085124.
140. Mak, K.F., et al., *Atomically thin MoS 2: a new direct-gap semiconductor.* Physical review letters, 2010. **105**(13): p. 136805.
141. Xu, X., et al., *Spin and pseudospins in layered transition metal dichalcogenides.* Nature Physics, 2014. **10**(5): p. 343-350.
142. Autieri, C., et al., *Limited Ferromagnetic Interactions in Monolayers of MPS3 (M= Mn and Ni).* The Journal of Physical Chemistry C, 2022. **126**(15): p. 6791-6802.
143. Basnet, R., et al., *Controlling magnetic exchange and anisotropy by non-magnetic ligand substitution in layered MPX3 (M= Ni, Mn; X= S, Se).* arXiv preprint arXiv:2205.04585, 2022.
144. Wang, W., et al., *Charge density wave instability and pressure-induced superconductivity in bulk 1 T− Nb S 2.* Physical Review B, 2020. **102**(15): p. 155115.
145. Wendumu, T.B., et al., *Optical properties of triangular molybdenum disulfide nanoflakes.* The Journal of Physical Chemistry Letters, 2014. **5**(21): p. 3636-3640.

146. Autieri, C., A. Bouhon, and B. Sanyal, *Gap opening and large spin–orbit splitting in (M= Mo, W; X= S, Se, Te) from the interplay between crystal field and hybridisations: insights from ab-initio theory.* Philosophical Magazine, 2017. **97**(35): p. 3381-3395.
147. Mak, K.F., et al., *Control of valley polarization in monolayer MoS 2 by optical helicity.* Nature nanotechnology, 2012. **7**(8): p. 494-498.
148. Xiao, F., et al., *Pressure-induced structural transition, metallization, and topological superconductivity in PdSSe.* Physical Review B, 2022. **105**(11): p. 115110.

Dostępy do artykułów:

Ghulam Hussain, Giuseppe Cuono, Rajibul Islam, Artur Trajnerowicz, Jarosław Jureńczyk, Carmine Autieri, Tomasz Dietl. *Electronic and optical properties of InAs/InAs$_{0.625}$Sb$_{0.375}$ superlattices and their application to far-infrared detectors,* Journal of Physics D: Applied physics **55**, 495301 (2022), https://doi.org/10.1088/1361-6463/ac984d

Ghulam Hussain, Mazia Asghar, Muhammad Waqas Iqbal, Hamid Ullah, Carmine Autieri. *Exploring the structural stability, electronic and thermal attributes of synthetic 2D materials and their heterostructures*, Applied Surface Science **590**, 153131 (2022), https://doi.org/10.1016/j.apsusc.2022.153131

Ghulam Hussain, Mumtaz Manzoor, Muhammad Waqas Iqbal, Imran Muhammad, Asadollah Bafekry, Hamid Ullah, Carmine Autieri. *Strain modulated electronic and optical properties of laterally stitched MoSi$_2$N$_4$/XSi$_2$N$_4$ (X=W, Ti) 2D heterostructures,* Physica E **144**, 115471 (2022), https://doi.org/10.1016/j.physe.2022.115471

Ghulam Hussain, Abdus Samad, Majeed Ur Rehman, Giuseppe Cuono, Carmine Autieri. *Emergence of Rashba splitting and spin-valley properties in Janus MoGeSiP$_2$As$_2$ and WGeSiP$_2$As$_2$ monolayers,* Journal of Magnetism and Magnetic Materials **563**, 169897 (2022), https://doi.org/10.1016/j.jmmm.2022.169897